

Surviving the Waves: evidence for a dark matter cusp in the tidally disrupting Small Magellanic Cloud

Michele De Leo,^{1,2,3}★ Justin I. Read,³ Noelia E. D. Noël,³ Denis Erkal,³ Pol Massana,^{4,3} Ricardo Carrera⁵

¹*Instituto de Astrofísica, Pontificia Universidad Católica de Chile, Av. Vicuña Mackenna 4860, 7820436, Macul, Santiago, Chile*

²*Instituto Milenio de Astrofísica MAS, Nuncio Monseñor Sotero Sanz 100, Of. 104, Providencia, Santiago, Chile*

³*Department of Physics, University of Surrey, Guildford, GU2 7XH, UK*

⁴*Department of Physics, Montana State University, P.O. Box 173840, Bozeman, MT 59717-3840, USA*

⁵*INAF - Osservatorio Astronomico di Padova, Vicolo dell'Osservatorio 5, 35122 Padova, Italy*

Accepted XXX. Received YYY; in original form ZZZ

ABSTRACT

We use spectroscopic data for ~6,000 Red Giant Branch (RGB) stars in the Small Magellanic Cloud (SMC), together with proper motion data from *Gaia* Early Data Release 3 (EDR3), to build a mass model of the SMC. We test our Jeans mass modelling method (BINULATOR+GRAVSPHERE) on mock data for an SMC-like dwarf undergoing severe tidal disruption, showing that we are able to successfully remove tidally unbound interlopers, recovering the dark matter density and stellar velocity anisotropy profiles within our 95% confidence intervals. We then apply our method to real SMC data, finding that the stars of the cleaned sample are isotropic at all radii (at 95% confidence) and that the inner dark matter density profile is dense, $\rho_{DM}(150 \text{ pc}) = 1.58^{+0.80}_{-0.58} \times 10^8 M_{\odot} \text{ kpc}^{-3}$, consistent with a Λ Cold Dark Matter (Λ CDM) cusp. Our model gives a new estimate of the SMC's total mass within 3 kpc ($M_{\text{tot}} \leq 3 \text{ kpc}$) of $2.29 \pm 0.46 \times 10^9 M_{\odot}$. We also derive an astrophysical “*J*-factor” of $18.99 \pm 0.16 \text{ GeV}^2 \text{ cm}^{-5}$ and a “*D*-factor” of $18.73 \pm 0.04 \text{ GeV}^2 \text{ cm}^{-5}$, making the SMC a promising target for dark matter annihilation and decay searches. Finally, we combine our findings with literature measurements to test models in which dark matter is “heated up” by baryonic effects. We find good qualitative agreement with the Di Cintio et al. 2014 model but we deviate from the Lazar et al. 2020 model at high $M_*/M_{200} > 10^{-2}$. We provide a new, analytic, density profile that reproduces dark matter heating behaviour over the range $10^{-4} < M_*/M_{200} < 10^{-1}$.

Key words: galaxies: individual: SMC – galaxies: evolution – galaxies: dwarf – Magellanic Clouds – galaxies: kinematics and dynamics – Dark Matter

1 INTRODUCTION

One of the long-standing problems of the prevailing Λ Cold dark matter (Λ CDM) cosmological model is the discrepancy between the observed constant density “cores” of gas rich dwarf galaxies ($\rho_{DM}(150 \text{ pc}) \sim \text{constant} \sim 5 \times 10^7 M_{\odot} \text{ kpc}^{-3}$; e.g. Moore 1994; Flores & Primack 1994; Read et al. 2017) and the dense “cusps” predicted by pure dark matter structure formation simulations ($\rho_{DM}(150 \text{ pc}) > 10^8 M_{\odot} \text{ kpc}^{-3}$; e.g. Dubinski & Carlberg 1991; Navarro et al. 1996b, 1997). Numerous solutions to this so-called “cusp-core problem” have been proposed, falling into three main categories. The first class of solution proposes new dark matter models, such as Self Interacting dark matter (Spergel & Steinhardt 2000), Warm dark matter (e.g. Hogan & Dalcanton 2000; Bode

et al. 2001; Avila-Reese et al. 2001), or “Wave-like” dark matter (e.g. Schive et al. 2014). The second class challenges the interpretation of the data in some cases, for example the existence of systematic errors due to the typically assumed spherical symmetry and circular gas motions (e.g. Read et al. 2016b; Genina et al. 2018; Oman et al. 2019). The third class proposes that “baryonic effects”, like repeated gas cooling and blowout through the starburst cycle, can kinematically “heat” the dark matter pushing it out of the centres of dwarf galaxies (e.g. Navarro et al. 1996a; Gnedin & Zhao 2002; El-Zant et al. 2001; Read & Gilmore 2005; Mashchenko et al. 2008; Pontzen & Governato 2012; Di Cintio et al. 2014a,b; Pontzen & Governato 2014; Orkney et al. 2021). This third class of solution has been gaining traction due to it making a number of testable predictions that are now supported by a host of observational data. dark matter heating models predict that star formation should be bursty, with a peak-to-trough burst amplitude of ~10, a burst duration shorter than the local dynamical time and a kinematically “hot”

★ E-mail: micheled189@gmail.com

stellar disc (e.g. [Teyssier et al. 2013](#); [Sparre et al. 2017](#)). The same models predict that stars should slowly migrate outwards ([Read & Gilmore 2005](#)), yielding an age gradient (e.g. [El-Badry et al. 2016](#)) and that cusp-core transformations need to take many dynamical times, meaning that dwarf galaxies with truncated star formation should be more cuspy than those with extended star formation (e.g. [Di Cintio et al. 2014a](#); [Read et al. 2016a](#)). All of these predictions have been borne out by data so far (e.g. [Kauffmann 2014](#); [Leaman et al. 2012](#); [Emami et al. 2019](#); [Zhang et al. 2012](#); [Read et al. 2019](#); [Collins & Read 2022](#)).

However, a key forecast of dark matter heating models has only recently been tested. Following [Peñarrubia et al. \(2012\)](#), [Di Cintio et al. \(2014a\)](#) parameterise the amount of cusp-core transformation a dwarf galaxy undergoes by its stellar-to-halo mass ratio, M_*/M_{200} . This works to leading order¹ because M_* is proportional to the total integrated supernova energy available to unbind the dark matter cusp, while M_{200} represents the potential well depth and, therefore, how much energy is required. [Di Cintio et al. \(2014a\)](#) predict cusped dwarfs for $M_*/M_{200} \lesssim 5 \times 10^{-4}$, cored dwarfs for $5 \times 10^{-4} \lesssim M_*/M_{200} \lesssim 5 \times 10^{-2}$, and cusped dwarfs again for $M_*/M_{200} \gtrsim 10^{-2}$, with this latter owing to the potential well depth winning over the energy available to unbind the cusp.² [Read et al. \(2019\)](#) measured the inner dark matter densities of 16 nearby dwarfs with $10^{-4} \lesssim M_*/M_{200} \lesssim 5 \times 10^{-3}$, finding excellent qualitative agreement with [Di Cintio et al. \(2014a\)](#). In a similar study, [Bouché et al. \(2022\)](#) probed $10^{-3} \lesssim M_*/M_{200} \lesssim 3 \times 10^{-2}$, finding results consistent with [Read et al. \(2019\)](#) where they overlap, and favouring a return cuspy galaxies at higher M_*/M_{200} , as predicted by [Di Cintio et al. \(2014a\)](#). However, [Bouché et al. \(2022\)](#) base their study on dwarfs at a redshift $z = 1$ that are not necessarily comparable with the local sample from [Read et al. \(2019\)](#). In this context, the Small Magellanic Cloud (SMC), with $M_*/M_{200} \sim 7 \times 10^{-3}$, and at a distance of $\sim 62 \pm 1.28$ kpc ([Graczyk et al. 2020](#)) from us poses a unique opportunity to test dark matter heating models at a higher M_*/M_{200} than previously probed for nearby dwarfs. The main challenge to using a standard equilibrium mass modelling method in this galaxy is the overwhelming evidence showing that the outskirts of the SMC are in fact tidally disrupted (e.g. [Evans & Howarth 2008](#); [Olsen et al. 2011](#); [Noël et al. 2013](#); [Ripepi et al. 2014](#); [Dobbie et al. 2014](#); [Noël et al. 2015](#); [Carrera et al. 2017](#); [Zivick et al. 2018, 2019](#); [Massana et al. 2020](#); [De Leo et al. 2020](#); [Zivick et al. 2021](#); [Niederhofer et al. 2021](#)). The hypothesis of heavy tidal disruption is also supported by the observations of distance-tracer populations such as classical Cepheids (i.e. [Jacyszyn-Dobrzniecka et al. 2016](#); [Scowcroft et al. 2016](#); [Ripepi et al. 2017](#)) and RR Lyrae (i.e. [Jacyszyn-Dobrzniecka et al. 2017](#); [Muraveva et al. 2018](#)) that show a long line-of-sight depth for the SMC.

Fortunately, there is no direct observational evidence that the tidal disruption extends to the inner regions of the SMC. It is thus possible to reconcile the observations of extended disruption

and long line-of-sight depth previously mentioned with equilibrium mass modelling by hypothesising that the SMC is composed of a bound remnant surrounded by an extended field of tidal debris. This bound remnant is not intended as a classical stellar bulge, but rather as the ensemble of all matter (dark matter, stars and gas) still bound by the SMC self-gravity. Due to the SMC being a dark matter dominated system, we expect this bound remnant to be dominated by the dark matter distribution and exhibit a roughly spherical shape. This would be the case even if the SMC possessed gaseous and stellar discs in its past as such structures don't survive tidal stirring and evolve into spherical distributions (i.e. [Kazantzidis et al. 2013](#), and references therein). The key to successfully model the galaxy's remnant then resides in the removal of the debris along the line of sight to the centre of the SMC that can contaminate the inner stellar kinematics (i.e. [Klimentowski et al. 2007](#)).

In this paper, we combine the unprecedented kinematic sample of ~ 6000 SMC stars from [De Leo et al. \(2020\)](#), which includes line of sight velocities and proper motions, with the Jeans modeling code GRAVSPHERE³ ([Read & Steger 2017](#); [Read et al. 2018](#); [Genina et al. 2020](#); [Collins et al. 2021](#)) to produce a new mass model of the SMC. We assume that the SMC's tidal disruption is not complete, such that the central bound region of the galaxy can be modelled assuming pseudo-dynamic equilibrium. We use a new binning module for GRAVSPHERE called the BINULATOR ([Collins et al. 2021](#)) to successfully remove contaminating, tidally unbound, stars along the line of sight to the SMC. To test our method, we apply the BINULATOR and GRAVSPHERE to mock data for a severely disrupting SMC, showing that even in this extreme case, we are able to correctly infer the stellar velocity anisotropy and inner dark matter density within our 95% confidence intervals. We then apply BINULATOR and GRAVSPHERE to the real SMC data to constrain the dark matter mass profile of the SMC, its pre-infall mass and to test dark matter heating models. We also determine whether the SMC is a promising target for dark matter annihilation and/or decay searches (e.g. [Caputo et al. 2016](#)).

This paper is organised as follows. In §2, we present the data used for the mass model. In §3, we discuss the GRAVSPHERE+BINULATOR mass modelling method. In §4, we present our results which we discuss in §5. Finally, we present our conclusions in §6.

2 DATA

In this section, we describe both the observational (§2.1) and simulation data (§2.2) that we use to generate the mock data for this study.

2.1 Observational data

We used spectroscopic data of RGB stars in the SMC area from the catalogues presented in [De Leo et al. \(2020\)](#) and [Dobbie et al. \(2014\)](#), the *Gaia* DR2 [Gaia Collaboration et al. \(2018\)](#) and EDR3 [Gaia Collaboration et al. \(2021\)](#) catalogues, and a photometric selection of RGB stars from the Survey of the MAGellanic Stellar History (SMASH, [Nidever et al. 2021](#)), cross-matched with *Gaia* EDR3.

³ Available here: <https://github.com/justinread/gravsphere>

¹ In practice, M_*/M_{200} is not fully sufficient on its own as it does not capture information about the size of the dark matter core (which is typically of order the half stellar mass radius, $R_{1/2}$; [Oñorbe et al. 2015](#); [Read et al. 2016a](#)), the burstiness of the star formation that actually took place, nor the impact of potential fluctuations driven by gas/stellar clumps and/or minor mergers (e.g. [El-Zant et al. 2001](#); [Orkney et al. 2021](#)). Nonetheless, M_*/M_{200} does appear to correlate well with the presence/absence of a core for most simulated dwarfs in a Λ CDM cosmology (e.g. [Di Cintio et al. 2014a](#)).

² This prediction may need to be revisited, however, if Active Galactic Nuclei in dwarfs provide an additional source of significant potential fluctuations (e.g. [Martizzi et al. 2013](#)).

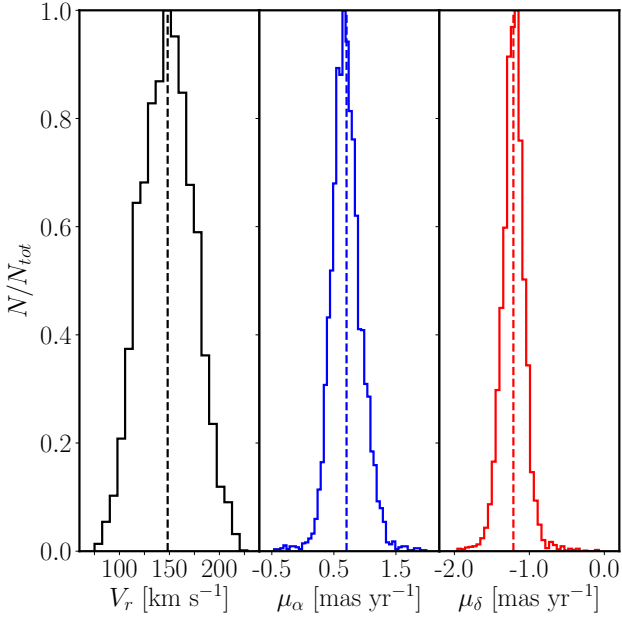


Figure 1. Kinematic distributions of our sample stars. Each panel shows a histogram that represents the distribution of one of the velocity components; the perpendicular dashed lines represent the mean values. The velocity components shown are the radial velocity V_r (in black in the *left panel*), the proper motion μ_α (in blue in the *middle panel*), and the proper motion μ_δ (in red in the *right panel*).

2.1.1 Radial velocities

We used the radial velocity determinations from the “extended” sample presented in De Leo et al. (2020) which also includes SMC RGB stars from Dobbie et al. (2014). For the full details of the analysis that led to the radial velocity determinations see De Leo et al. (2020). Briefly, the raw spectra acquired with the 2dF+AAOmega instrument at the AAT were processed with the 2dfdr tool⁴ (Sharp & Birchall 2010) and proprietary software to reduce them, remove sky contamination, subtract the solar reflex motion and finally derive radial velocities through cross-correlation with a grid of synthetic spectra (details of the grid in Allende Prieto et al. 2018). This sample includes ~ 6000 RGB stars which are confirmed SMC members (i.e. with radial velocities V_r between 70 and 230 km s⁻¹). The distribution of radial velocities can be seen on the left panel of Fig. 1 where the large velocity dispersion of the system (c.f. Hatzidimitriou et al. 1993; Harris & Zaritsky 2006) is clearly appreciated.

2.1.2 Proper motions

We cross-matched the radial velocity sample presented above with the *Gaia* EDR3 catalogue. For discussions on the systematics of *Gaia* see Lindegren et al. (2018), the recommendations from L. Lindegren⁵ and Lindegren et al. (2021). The total error budget for the proper motions in *Gaia* is as follows:

$$\sigma_{tot} = \sqrt{k^2 \sigma_i^2 + \sigma_s^2} \quad (1)$$

⁴ See <https://www.aao.gov.au/science/software/2dfdr>

⁵ IAU 30 GA *Gaia* 2 astrometry talk, available in extended version at <https://www.cosmos.esa.int/web/gaia/dr2-known-issues>.

where k is a factor accounting for the underestimation of the observational uncertainties, σ_i is the measured uncertainty for the i -th star and σ_s is the systematic error. The main difference with the data presented in De Leo et al. (2020) (which used proper motions from *Gaia* DR2) is in the lower observational uncertainties and systematics of *Gaia* EDR3 which translated into an improvement of about 65% in the systematic error σ_s and total uncertainties which are on average 47% and 35% smaller, respectively for $\mu_\alpha \cos \delta$ and μ_δ . Throughout the paper we will refer to the proper motion $\mu_\alpha \cos \delta$ simply as μ_α . As done in De Leo et al. (2020), we corrected the proper motion measurements to account for the solar reflex motion and for geometric effects (systematic contraction/expansion with respect to the centre due to the motion along the line of sight) following van de Ven et al. (2006) and Bianchini et al. (2018):

$$\mu_r = -6.1363 \times 10^{-5} V_{los} \frac{R}{d} \quad (2)$$

where μ_r is the correction in mas yr⁻¹, V_{los} is the velocity along the line of sight in km s⁻¹, R is the distance to the centre of the SMC in arcmin and d is the distance between the SMC and the Sun in kpc. The distributions of proper motions can be seen in blue (μ_α) and in red (μ_δ) respectively in the middle and right panels of Fig. 1. Both distributions show long tails and the distribution of μ_α (the blue histogram in the middle panel) shows larger dispersion and asymmetry favouring proper motions higher than the mean.

2.1.3 Stellar surface density

The kinematic sample presented above (radial velocities plus proper motions) was too small and incomplete to provide a reliable estimation of the stellar surface density. To have a more complete sampling of the inner regions of the SMC we derived the stellar surface density from a selection of RGB stars from SMASH, crossmatched with *Gaia* EDR3 (a sample from Massana et al. 2020). Using the deep photometry of SMASH and proper motions and parallaxes from *Gaia* EDR3 for foreground decontamination, we produced an accurate density profile of upper RGB bona-fide SMC candidates out to $\sim 11^\circ$ from the centre of the galaxy (that for this sample is at $\alpha_c, \delta_c = 13.16^\circ, -72.80^\circ$). The density is computed first counting the number of stars in each HEALPix⁶ (Górski et al. 2005; Zonca et al. 2019) pixel (nside=512), then dividing the SMC projected surface in equal-radius (0.3) annuli centred on (α_c, δ_c) and averaging the number of stars over the pixels included in each given annulus (taking into account that all pixels have equal area). Given the large number of RGB stars present in the SMASH sample, we were able to compute statistical uncertainties on the average values by taking the standard deviations in each annulus. This provided an accurate stellar surface density profile based on the same type of stars of our kinematics tracers and useful over large radii (see Figure 2).

2.2 Simulation data

In order to test our analysis method and mass model, we used two SMC-analogues taken from the suite of simulations presented in De Leo et al. (2020). One is a “bound” SMC that has undergone little tidal stripping. The other is a “heavily disrupted” SMC that is close to full dissolution. This latter is closest to the real SMC data though is likely more extreme. In particular, it starts out close to the SMC’s *current* inner velocity dispersion before tidal stripping and shocking.

⁶ <http://healpix.sourceforge.net>

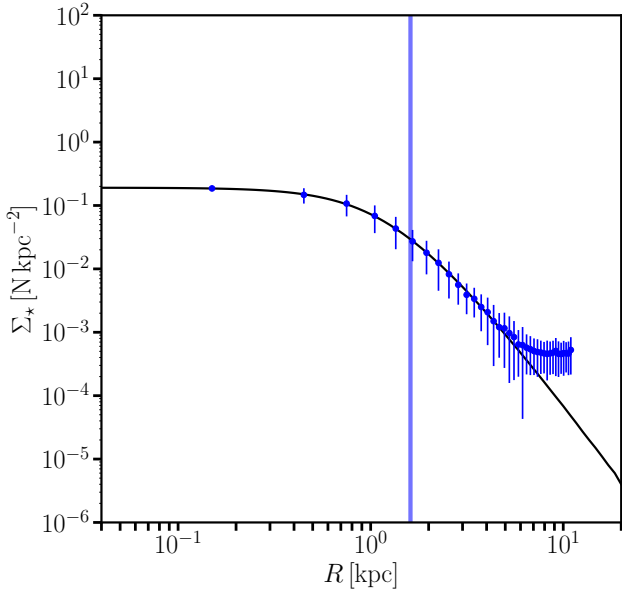


Figure 2. Surface number density profile, $\Sigma_*(r)$, of the SMASH sample of RGB stars cross-matched with Gaia EDR3 (Massana et al. 2020). The black line is the best fit model from GRAVSPHERE, the blue points with 68% confidence intervals are the profile computed from real data, and the fainter blue vertical line is the half-light radius computed by GRAVSPHERE.

As such, its final inner velocity dispersion is substantially colder than the true SMC data. This is nonetheless perfectly acceptable for testing our methodology.

The simulation setup is described in detail in De Leo et al. (2020). Here, we briefly summarise the key points. We ran a grid of N -body simulations using GADGET-3 (an updated version of GADGET-2; Springel 2005) with a live SMC (10^5 particles, a total mass of $M_{\text{SMC}} = 10^9 M_{\odot}$, and two different scale radii, as outlined below) modelled as a Plummer sphere (Plummer 1911) disrupting around a $1.5 \times 10^{11} M_{\odot}$ LMC (Erkal et al. 2019) in the presence of the Milky Way (modelled using the MWPotential2014 model from Bovy 2015). As specified in the original paper, the initial mass used for the SMC is based on its present-day dynamical mass (i.e., Harris & Zaritsky 2006), substantially lower than its likely peak mass before infall ($\sim 5 \times 10^{10} M_{\odot}$; Read & Erkal 2019). This is motivated by the fact that the simulations were not meant to faithfully model the entire disruption history of the SMC but only its final phases, once the SMC had lost the majority of its dark matter (Smith et al. 2016). The two simulations selected for the analysis in this work are at the opposite ends of the spectrum of explored scale radii, the most bound (0.8 kpc initial scale radius) and the most disrupted (1.5 kpc initial scale radius) SMC-analogues. The former bound SMC is used to test that the method works properly and is able to recover the true density profile in the absence of disrupting influences; the latter heavily disrupted SMC is the closest analogue to our observed case and likely, in fact, more extreme (see Figure 3 for a visual representation).

In De Leo et al. (2020) we have shown how the heavily disrupted simulation qualitatively reproduces the kinematic trends of the dispersion of the velocity distributions of the real SMC (visible here by comparing the top left panel of Fig. 6, for the heavily disrupted simulation, and the left panel of Fig. 8, for the real SMC). Figure 3 highlights how the debris field of tidally disrupted sim-

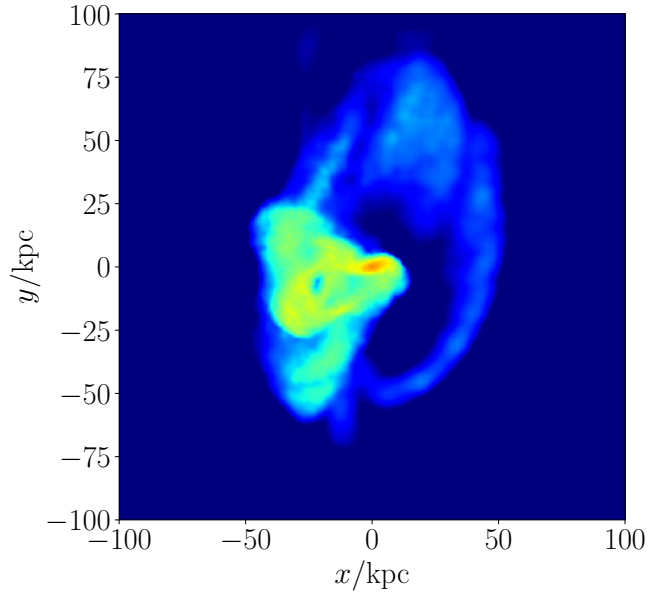


Figure 3. Density map of the heavily disrupted simulation (De Leo et al. 2020) projected on the XY -plane of the simulation phase space and centred on its photometric centre. Blue pixels have no particles in them. The density increases from cyan to light green, yellow and orange for the densest regions in the centre. The cyan and light green plumes and arcs trace the past orbit of the simulated galaxy and are composed of particles making up tidal debris around the central bound remnant of the galaxy.

ulation particles (low density cyan and blue-ish) is widely spread, covering tens of kpc in the sky. To further prove the similarity of the heavily disrupted simulation with the real SMC morphology, we computed the projected-on-the-sky ellipticity of both (ignoring the distance information of the simulation, unavailable for the real SMC). Following Bruderer et al. (2016), we obtained a projected ellipticity of 0.962 using the tracers within 1 kpc of the centre for the simulation data at the final snapshot, which compares well to the 0.943 at the same radius obtained for the real SMC data with the same technique.

Both the observed and the simulation data were treated with the same analysis pipeline and mass modeling tool. This procedure included adding errors for the simulation data resembling the observational ones. The errors for the simulation data were sampled from Gaussians for each observable (V_r , μ_{α} or μ_{δ}). The results of this procedure can be seen in Fig. 4, where in each panel the black histograms are the observed errors (left panel for Err_{V_r} , middle panel for $\text{Err}_{\mu_{\alpha}}$ and right panel for $\text{Err}_{\mu_{\delta}}$) and the red dot-dashed lines are the Gaussians sampled to generate the simulation errors.

Regarding the errors for the simulation data, it is important to keep in mind that, as pointed out in De Leo et al. (2020), the simulated SMC analogues are less massive than the real SMC, leading to kinematically cooler velocity dispersion profiles (see also the discussion, above). Thus, when drawing our errors from the real SMC observations, we overestimate the fractional uncertainty on the simulated dispersion profiles. This means that our mock data present a worst-case scenario for testing our analysis pipeline.

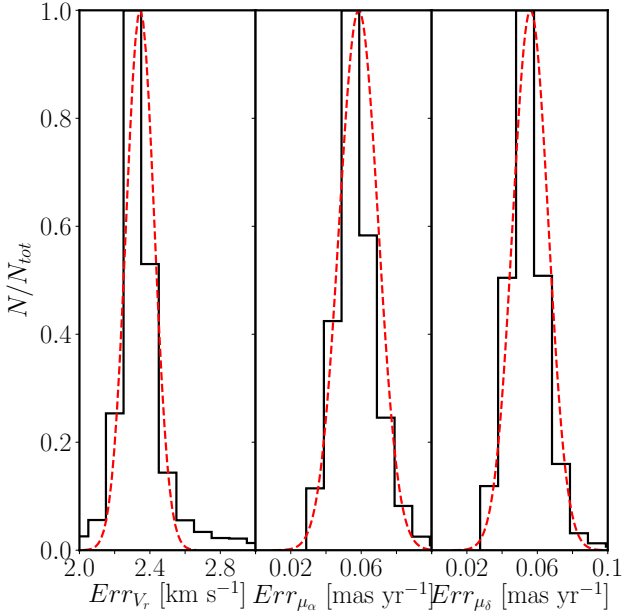


Figure 4. Distributions of the observed errors for the real SMC data (black histograms) and Gaussians from which the errors for the simulated mock SMC-analogues are sampled (red dash-dotted lines). Each panel shows a different variable: V_r (left panel), μ_α (middle panel), and μ_δ (right panel).

3 MASS MODELLING

3.1 GRAVSPHERE

Our mass modelling technique is based on solving the spherical Jeans equation (e.g. Jeans 1922; Binney 1980; Binney & Tremaine 2008):

$$\frac{1}{v} \frac{\partial}{\partial r} (v \sigma_r^2) + \frac{2\beta(r)\sigma_r^2}{r} = -\frac{GM(<r)}{r^2} \quad (3)$$

where $v(r)$ is the kinematic tracer density; $\sigma_r^2 = \langle v_r^2 \rangle - \langle v_r \rangle^2$ is the velocity dispersion of the tracers; $G = 6.67398 \times 10^{-11} \text{ m}^3 \text{ kg}^{-1} \text{ s}^{-2}$ is Newton’s gravitational constant; $M(<r)$ is the total mass inside spherical radius r ; and $\beta(r) = 1 - \sigma_t^2/\sigma_r^2$ is the velocity anisotropy, where σ_t is the tangential velocity dispersion. This equation is valid under the assumptions of no rotation (which we excluded for the SMC RGB population in De Leo et al. 2020), dynamical equilibrium, and spherical symmetry. We will test these latter two assumptions with mock data in §2.2.

We solve equation 3 using the GRAVSPHERE code with the aim of recovering the total cumulative mass (stars and dark matter), the dark matter density profile $\rho_{DM}(r)$ and the stellar velocity anisotropy profile $\beta(r)$ of the object being studied. The full methodology is described and tested in detail in Read & Steger (2017); Read et al. (2018); Genina et al. (2020); Read et al. (2021); Collins et al. (2021). The code is publicly available⁷ and has already been used to model a wide range of nearby spherical stellar systems (e.g. Read et al. 2018, 2019; Collins et al. 2021; Zoutendijk et al. 2021a). Here, we briefly summarise the main points.

Eq. 3 is integrated along the line of sight to obtain expressions for the line of sight, radial and tangential velocity dispersions, as a

function of projected distance, R (e.g. Binney & Mamon 1982; van der Marel 1994; Mamon & Łokas 2005):

$$\sigma_{LOS}^2 = \frac{2}{\Sigma_*(R)} \int_R^\infty \left(1 - \beta(r) \frac{R^2}{r^2}\right) \frac{v(r)\sigma_r^2(r)r}{\sqrt{r^2 - R^2}} dr \quad (4)$$

$$\sigma_{POSr}^2 = \frac{2}{\Sigma_*(R)} \int_R^\infty \left(1 - \beta(r) + \beta(r) \frac{R^2}{r^2}\right) \frac{v(r)\sigma_r^2(r)r}{\sqrt{r^2 - R^2}} dr \quad (5)$$

$$\sigma_{POS_t}^2 = \frac{2}{\Sigma_*(R)} \int_R^\infty (1 - \beta(r)) \frac{v(r)\sigma_r^2(r)r}{\sqrt{r^2 - R^2}} dr \quad (6)$$

where σ_{LOS} , σ_{POSr} and σ_{POS_t} are the tracers’ line of sight, projected radial and projected tangential velocity dispersions; $\Sigma_*(R)$ is the tracers’ surface density at the projected radius R ; and

$$\sigma_r^2(r) = \frac{1}{v(r)g(r)} \int_r^\infty \frac{GM(\tilde{r})v(\tilde{r})}{\tilde{r}^2} g(\tilde{r}) d\tilde{r} \quad (7)$$

with:

$$g(r) = \exp\left(2 \int \frac{\beta(r)}{r} dr\right) \quad (8)$$

GRAVSPHERE has the possibility of additionally using two Virial Shape Parameters (VSP1 and VSP2) that constrain the global kurtosis of the stellar distribution, allowing the degeneracy between the cumulative mass and the velocity anisotropy, present if only line-of-sight velocity data are available, to be broken (e.g. Merrifield & Kent 1990; Richardson & Fairbairn 2014; Read & Steger 2017). However, for the SMC we have excellent constraints on σ_{LOS} , σ_{POSr} and σ_{POS_t} that also break this same degeneracy (e.g. Strigari et al. 2007; Read & Steger 2017). A key challenge in measuring VSPs for the SMC is that they formally require an integral over the kurtosis to infinity. This means that the kurtosis needs to be reliably measured at large radii where it could be strongly impacted by tides (e.g. De Leo et al. 2020). For mildly disrupting dwarfs, Read et al. (2018) show that an unbiased estimate of the VSPs can still be obtained by extrapolating the kurtosis to large radii from constraints further in. Using a similar approach, we were able to recover VSP1 for both the mock and real SMC data, but VSP2 – that is more sensitive to data further out – was very poorly constrained and so we do not use it in this paper.

GRAVSPHERE has evolved significantly since its first tests in Read & Steger (2017) and Read et al. (2018). The version we used here is the one presented in Collins et al. (2021). The most important changes were put in place to counteract a small bias in the density beyond $\sim 4R_{1/2}$ (Read & Steger 2017; Read et al. 2021), and biases introduced by the binning method in the presence of a small number of tracers or large velocity errors (Gregory et al. 2020; Zoutendijk et al. 2021b; Collins et al. 2021). These prompted the development of the BINULATOR as a separate code to handle the data binning, and a switch of the mass model from a “non-parametric” series of power laws centred on radial bins to the CORENFWTIDES profile (Read et al. 2018; Read & Erkal 2019). The two profiles have been shown to yield constraints on the cumulative mass profile that are statistically consistent with one another (Alvarez et al. 2020). However, the CORENFWTIDES density profile, $\rho_{cNFWt}(r)$, has the advantage of producing profiles that more easily connect to parameters of interest in cosmological models:

$$\rho_{cNFWt}(r) = \begin{cases} \rho_{cNFW} & r < r_t \\ \rho_{cNFW}(r_t) \left(\frac{r}{r_t}\right)^{-\delta} & r > r_t \end{cases} \quad (9)$$

⁷ <https://github.com/justinread/gravsphere>.

where r_t sets the radius at which mass is tidally stripped from the galaxy, δ sets the logarithmic density slope beyond r_t ; ρ_{cNFW} is given by:

$$\rho_{\text{cNFW}}(r) = f^n \rho_{\text{NFW}} + \frac{n f^{n-1} (1 - f^2)}{4\pi r^2 r_c} M_{\text{NFW}}; \quad (10)$$

$$M_{\text{cNFW}}(< r) = M_{\text{NFW}}(< r) f^n; \quad (11)$$

the function f^n generates a shallower profile below a core-size parameter, r_c :

$$f^n = \left[\tanh\left(\frac{r}{r_c}\right) \right]^n; \quad (12)$$

and $M_{\text{NFW}}(< r)$ is the cumulative mass of the ‘Navarro, Frenk & White’ (NFW) profile (Navarro et al. 1996b):

$$M_{\text{NFW}}(r) = M_{200} g_c \left[\ln\left(1 + \frac{r}{r_s}\right) - \frac{r}{r_s} \left(1 + \frac{r}{r_s}\right)^{-1} \right]; \quad (13)$$

$$g_c = \frac{1}{\log(1 + c_{200}) - \frac{c_{200}}{1 + c_{200}}}; \quad (14)$$

$$r_{200} = \left[\frac{3}{4} M_{200} \frac{1}{\pi \Delta \rho_{\text{crit}}} \right]^{1/3}; \quad (15)$$

where c_{200} is the dimensionless *concentration parameter*; $\Delta = 200$ is the over-density parameter; $\rho_{\text{crit}} = 136.05 M_{\odot} \text{ kpc}^{-3}$ (in a Λ CDM cosmology) is the critical density of the Universe at redshift $z = 0$; r_{200} is the virial radius at which the mean enclosed density is $\Delta \times \rho_{\text{crit}}$; and M_{200} is the virial mass – the mass within r_{200} .

In GRAVSPHERE, the cumulative mass profile $M(r)$ is given by the sum of the stellar mass profile $M_*(r)$, which is assumed to follow the tracer distribution with a flat prior on the total stellar mass $3.45 \times 10^8 M_{\odot} < M_* < 5.75 \times 10^8 M_{\odot}$ (McConnachie 2012), and the CORENFWTIDES profile (equation 9) for the dark matter. Our priors on the model parameters are reported in the first six rows of Table 1.

The tracer density is given by a sum of a series of N_p Plummer spheres (Plummer 1911; Rojas-Niño et al. 2016):

$$v = \sum_j^{N_p} \frac{3M_j}{4\pi a_j^3} \left(1 + \frac{r^2}{a_j^2}\right)^{-5/2} \quad (16)$$

where M_j and a_j are the mass and scale length of each individual component. $\Sigma_*(R)$ appears in Eqs. 4, 5, and 6 and has to be compared with the data. Eq. 16 makes $\Sigma_*(R)$ analytic:

$$\Sigma_*(R) = M_* \sum_j^{N_p} \frac{M_j}{\pi a_j^2} \left(1 + \frac{R^2}{a_j^2}\right)^{-2} \quad (17)$$

Typically, $N_p = 3$ is enough to model the tracer density, especially since the masses are allowed to be negative (under a constraint that the total density at all radii remains positive; Rojas-Niño et al. 2016). Rows 7 and 8 of Table 1 report the parameter space that the code searched when fitting the tracer densities for the models. The BINULATOR does a first fit of the tracer density and then GRAVSPHERE searches for a new solution around the best fit within a preset tolerance (here chosen to be 10^{-3} , as the data are very constraining).

The velocity anisotropy profile follows Baes & van Hese (2007) and Read & Steger (2017):

$$\beta(r) = \beta_0 + (\beta_{\infty} - \beta_0) \frac{1}{1 + (r_0/r)^{\eta}} \quad (18)$$

		Simulation run		Observation run	
	Parameter	Minimum	Maximum	Minimum	Maximum
1	$\log_{10}(M_{200})$	5.5	11.5	7.5	11.5
2	c_{200}	1.0	100.0	7.43	52.63
3	$\log_{10}(r_c)$	0.01	100.0	0.01	10.0
4	n	-1.0	1.0	-1.0	1.0
5	$\log_{10}(r_t)$	0.1	10.0	1.0	20.0
6	δ	3.01	8.0	3.01	8.0
7	$\frac{M_{1,2,3}}{M_*}$	-100	100	-5	5
8	$a_{1,2,3}$	0.01	2.0	0.1	2.5
9	$\log(r_0)$	-2.0	1.0	-2.0	0.0
10	η	1.0	3.0	1.0	3.0
11	β_0	-0.1	0.1	-0.3	0.3
12	β_{∞}	-0.1	1.0	-0.3	1.0
13	μ_v	-50	50	-50	50
14	α_v	4.0	15.0	10	60.0
15	β_v	1.0	5.0	1.0	5.0
16	A_1	0.0001	0.35	0.0001	0.35
17	μ_1	20.0	95.0	20.0	95.0
18	σ_1	30.0	125.0	30.0	125.0
19	A_2	0.0001	0.35	0.0001	0.35
20	μ_2	-95.0	-20.0	-95.0	-20.0
21	σ_2	30.0	125.0	30.0	125.0

Table 1. Bounds on the priors and parameters used by GRAVSPHERE and the BINULATOR. *The first six rows* are the bounds of the flat priors assumed for the mass profile. M_{200} is in M_{\odot} , c_{200} , n and δ are dimensionless, r_c and r_t are in kpc. *Rows 7 and 8* are the priors of the Plummer spheres used to fit the tracers density, with the M_j/M_* dimensionless (as the surface density data are normalised to integrate to 1) and a_j in kpc. *Rows from 9 to 12* are the priors for the anisotropy profile parameters where r_0 is in kpc and η , β_0 , and β_{∞} are dimensionless. *Rows 13 to 15* are the bounds of the parameter space searched for the fit of the residual velocity distributions. *Rows 16 to 21* are the parameters of the two secondary Gaussians used to model the contaminants of the velocity distributions (a standard Gaussian of amplitude A_i , mean μ_i , and dispersion σ_i).

where β_0 is the anisotropy at the centre, β_{∞} is the value at infinity, r_0 is the transition radius, η dictates the steepness of the profile, and the priors for all the parameters are given in rows 9 to 12 of Table 1. This definition of anisotropy allows for a wide range of anisotropy profiles while making Eq. 8 analytic. Even more general analytic forms are discussed and presented in Read & Steger 2017.

$\beta(r)$, as defined above, has values over an infinite range ($-\infty < \beta < 1$) which is problematic for model fitting and, hence, GRAVSPHERE uses instead a symmetrised version (Read et al. 2006b):

$$\tilde{\beta} = \frac{\sigma_r^2 - \sigma_t^2}{\sigma_r^2 + \sigma_t^2} = \frac{\beta}{2 - \beta} \quad (19)$$

With this definition, the anisotropy is bounded on a finite parameter space: $\tilde{\beta} = 1$ is full radial anisotropy, $\tilde{\beta} = 0$ is isotropy and $\tilde{\beta} = -1$ is full tangential anisotropy.

GRAVSPHERE fits the tracers’ surface density (Eq. 17) and velocity dispersion profiles (Eq. 4, Eqs. 5 and 6) using the MCMC code EMCEE (Foreman-Mackey et al. 2013). These fits allow for the reconstruction of the dark matter density and stellar velocity anisotropy profiles through the other equations presented here.

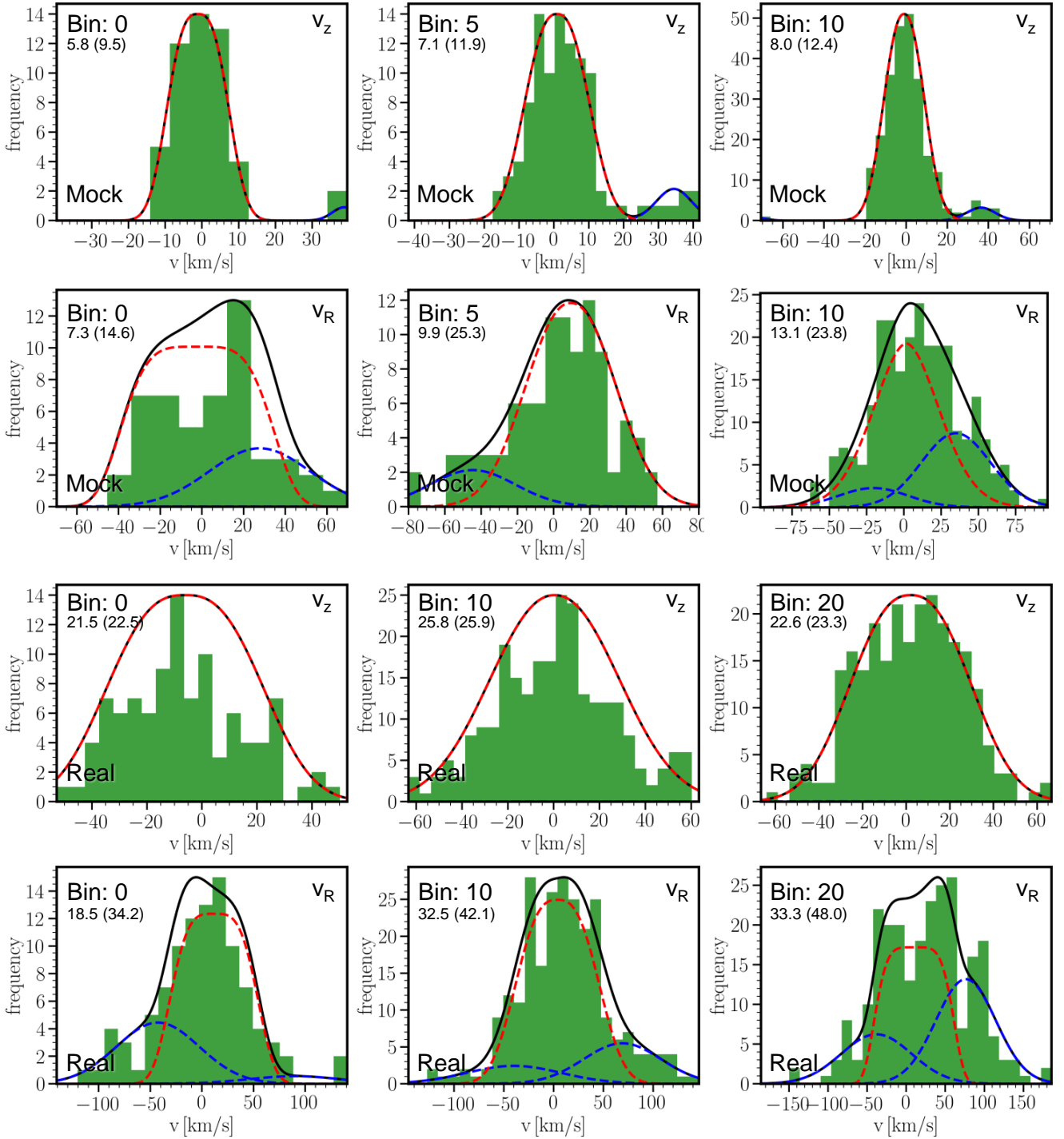


Figure 5. The velocity distribution functions (VDFs) of some of the bins of the heavily disrupted SMC-analogue (top two rows) and of the real SMC (bottom two rows). In each panel, the VDFs are the green histograms, the best BINULATOR fit to the distribution (including both the main SMC generalised Gaussian and the secondaries representing the debris) the solid black line, the fit to the SMC the dashed red line and the secondary distributions for the debris the dashed blue lines. The numbers reported below the bin identifier in the top left corner of each panel are the dispersion of the SMC distribution: the first number is the dispersion recovered by the BINULATOR fit, the number in brackets is the dispersion that would be recovered by fitting the entire bin with a single component (so without any distinction between SMC and debris). *First and third row:* In the VDFs for the LOS velocity distribution, v_z , the debris are clearly identifiable and removed for the simulation (first row) and do not affect the real SMC data distribution (third row). *Second and fourth row:* the VDFs along the radial direction on the plane of the sky, v_R , the debris are more difficult to disentangle from the bulk SMC distribution for both simulation (second row) and real SMC data (fourth row). The tangential direction on the plane of the sky, v_T , is omitted as it shows similar behaviour to v_R .

3.2 The BINULATOR

In [Collins et al. \(2021\)](#), the binning routines of `GRAVSPHERE` were redeveloped and built into their own code, the `BINULATOR`. This implements one main change: each projected radial bin (that contains an equal number of stars, weighted by their membership probability) is fit with a generalised Gaussian, convolved with the error PDF of each star:

$$p_i = \frac{\beta_v}{2\tilde{\alpha}_v\Gamma(1.0/\beta_v)} \exp\left(-\frac{|v_i - \mu_v|}{\tilde{\alpha}_v}\right) \quad (20)$$

where:

$$\tilde{\alpha}^2 = \alpha_v^2 + \sigma_{e,i}^2 \frac{\Gamma(1.0/\beta_v)}{\Gamma(3.0/\beta_v)} \quad (21)$$

and $\sigma_{e,i}$ is the width of the PDF of the error on the i -th star; v_i is the velocity (be it line-of-sight or along one of the plane of the sky directions) of the i -th star; $\Gamma(x)$ is the Gamma Function; and μ_v , α_v and β_v are parameters fit to each bin. These allow us to recover the mean, μ_v , variance, $\sigma_v^2 = \alpha_v^2\Gamma(3.0/\beta_v)/\Gamma(1.0/\beta_v)$ and kurtosis, $k = \Gamma(5.0/\beta_v)\Gamma(1.0/\beta_v)/[\Gamma(3.0/\beta_v)]^2$, of that bin (c.f. the similar method in [Sanders & Evans 2020](#)). Note that the above is an analytic approximation to the true convolution integral. [Collins et al. \(2021\)](#), their Figure 10) show that this matches the true convolution integral at typically better than 5% accuracy, and rarely more poorly than 10%. Rows 13 to 15 of Table 1 list the priors used for the fit of the velocity PDFs for the real and simulated data.

3.3 Removing tidal debris

Due to the heavy tidal disruption, the SMC is currently undergoing, the kinematic sample is likely contaminated by unbound debris which invalidates the assumption of dynamical equilibrium required for the modelling. This is a problem long-recognised in the literature (i.e. [Klimentowski et al. 2007](#)), made particularly challenging by the fact that the debris stars are chemically similar to the bound stars. A standard solution is to sigma clip stars with anomalously high velocities (i.e. [Wilkinson et al. 2004](#); [Klimentowski et al. 2007](#)). However, this raises the spectre that genuine member stars are accidentally removed, impacting estimates of both the dispersion and, in particular, the kurtosis that is sensitive to the wings of the velocity distribution function. Furthermore, it is hard to marginalise over ambiguous stars that may or may not be bound, since they must be either in or out.

Here, we use the `BINULATOR` to remove the tidal debris by representing the debris with up to two secondary Gaussians (bounds on their parameters in rows 16 to 21 of Table 1) that we add to the velocity distribution function in equation 20. These secondary Gaussians are forced to have a mean distinct from zero (one positive and one negative, for debris on each side of the main velocity distribution), and can have a negligible amplitude. These choices ensure the debris distributions are separate from the bulk motion of the SMC (at mean zero), and also that the secondary Gaussians can be present or absent independently from each other in each bin. This allows us to fully marginalise over the bound member stars when `BINULATOR` fits its velocity distribution function bin by bin. The `BINULATOR` transforms the observed velocities on the plane of the sky in the radial and tangential components with respect to the centre of the SMC, so $(V_r, \mu_\alpha, \mu_\delta)$ becomes (V_z, V_R, V_T) , and the velocity distribution in each direction is fitted independently. We test this idea using mock data drawn from our heavily disrupted simulated SMC-analogue in §4.1.1. An example fit of `BINULATOR`'s "generalised Gaussian + secondary Gaussians" PDF to some of the

bins for the heavily disrupted mock (top two rows) and the real SMC (bottom two rows) is shown in Fig. 5. In each panel, the velocity distribution is in green, the sum of the Gaussians is the solid black line, the fit to the SMC distribution is the dashed red line and the secondary Gaussians for the debris are the blue dashed lines. The numbers in the top left corner of each panel, below the bin identifier, are the dispersion for that bin recovered by the `BINULATOR` and, in brackets, the dispersion recovered by fitting a single component to the whole bin (thus without any distinction between the distributions of the main SMC and of the debris). The difference between these two recovered values gives a gauge of the importance of the removal of the contamination due to the tidal debris. As can be seen from the figure, the debris are easily recognisable and removed in the LOS velocity distributions (V_z , first and third row of the figure) but are more difficult to disentangle from the bulk SMC motion in the radial component on the plane of the sky (V_R , second and fourth row, the tangential component V_T shows the same behaviour as V_R). This difference in the overall effect and severity of the debris' contamination leads our model to be more tightly constrained by the LOS data and to larger errors in the estimated distributions in the plane of the sky directions. It is important to note that we do not actually use the best-fit velocity distribution function found by `BINULATOR` to generate the velocity dispersion profiles and their uncertainties, but rather we use the median and 68% confidence intervals of the distribution of the many fits that the `BINULATOR` does for each bin (to marginalise over model degeneracies).

4 RESULTS

4.1 Tests on the simulated SMC-analogues

Before applying our methodology (§3) to the real SMC data, we first test it on simulated mock SMC analogues. We consider two mocks, as described in §2.2: a bound SMC that has undergone very little tidal disruption, and a heavily disrupted SMC that is close to dissolution. This latter is closer to the real situation, but likely even more extreme as the mock SMC has a starting mass lower than the original mass of the SMC (as reconstructed via abundance matching, i.e. in [Read & Erkal 2019](#)). As such, it represents a conservative test-case. We first assess how well `BINULATOR` can remove unbound tidal debris along the line of sight (§4.1.1); we then apply `GRAVSPHERE` to the mock data to determine how well we can recover the inner dark matter density profile and stellar velocity anisotropy (§4.1.2). Other profiles recovered by our models are reported in Appendix A for completeness.

4.1.1 Testing the removal of tidal debris

In Fig. 6, we show the velocity dispersion profiles derived from the heavily disrupted simulation. In the top left panel, we show the results including all data, both bound and unbound stars. In the top right panel, we show results for the same simulation but clipping all data beyond 2 standard deviations from the dispersion derived for each bin (2σ -clipped), assuming the original velocity distributions to be Gaussians (see Fig. 1). In the bottom left panel, we show the results obtained by removing the stars with a velocity above the escape velocity V_{esc} at their respective position (i.e. the unbound stars).

$$V_{esc} = \sqrt{-2\Phi(r)} \quad (22)$$

$$\Phi(r) = -G \int_r^\infty \frac{M(<r)}{r'^2} dr' \quad (23)$$

with $\Phi(r)$ the gravitational potential, $M(r)$ tabulated from the particle data to a very high distance and the integral estimated numerically. Due to the advanced stage of tidal disruption of the simulation and the discrete mass distribution of the simulation particles, we iterated the selection process until it stopped removing particles. Finally, in the bottom right panel of Fig. 6, we show the profiles derived by the BINULATOR. The colours of the points in the bottom panels are different because the BINULATOR transformed the proper motions into the radial and tangential velocities on the plane of the sky and we did the same for the escape velocity cut sample, for ease of comparison (the better kinematically behaved, i.e. bound, sample will always have lower values of the velocity dispersions anyway). As can be seen from the bottom left panel, when removing the stars with a velocity higher than the escape velocity, the inner dispersion profiles become consistent with one another: the inner velocity dispersion of bound stars is isotropic. Sigma clipping of the data in each bin (top right panel) is unable to reproduce this behaviour, with the 2σ -clipped dispersions remaining significantly tangentially anisotropic, even in the innermost bin. The BINULATOR (bottom right panel), however, is able to recover the correct behaviour within its statistical uncertainties by removing the unbound stars. The slight rise outward in the dispersions, along all velocities, that both the escape velocity cut sample (bottom left panel) and the BINULATOR (bottom right panel) exhibit is likely due to the physical onset of tides (Read et al. 2006a,b).

4.1.2 Testing the mass modelling

In this section, we now apply GRAVSPHERE to model the mock data surface brightness and velocity dispersion profiles extracted using BINULATOR (§3.3). The results for the bound simulation that has not experienced any significant tidal forces are shown in the top row of Fig. 7 while the bottom row is for the heavily disrupted simulation. The left and right columns of the figure show the recovered median (black line), 68% (dark grey), and 95% (light grey) confidence intervals for $\rho(r)$ and $\beta(r)$, respectively, as compared to the true solutions (blue data points and dashed lines). As can be seen, GRAVSPHERE correctly recovers all three within its 95% confidence intervals.

Fig. 7 shows that GRAVSPHERE is able to recover the density and velocity anisotropy profiles within its 95% confidence intervals for both the bound simulation (top panels) and the heavily disrupted simulation (bottom panels) within the half-stellar mass radius (vertical blue line, $R_{1/2}$). Beyond $R_{1/2}$, the recovered density profile is biased high for the heavily disrupted simulation as compared to the true solution (see Fig. 7, bottom left panel), while the velocity anisotropy profile also fluctuates slightly outside of the 95% confidence intervals (bottom right panel). This behaviour is to be expected given that the heavily disrupted simulation becomes unbound beyond $R_{1/2}$, with the percentage of bound stars quickly dropping below 90% outside 1.7 kpc.

4.2 Mass modelling of the real SMC

In this section, we show and discuss the principal results of our modelling of the SMC, namely the successful decontamination with the BINULATOR, the recovery of the mass density and velocity anisotropy profile and further insights derived from these two variables. Other

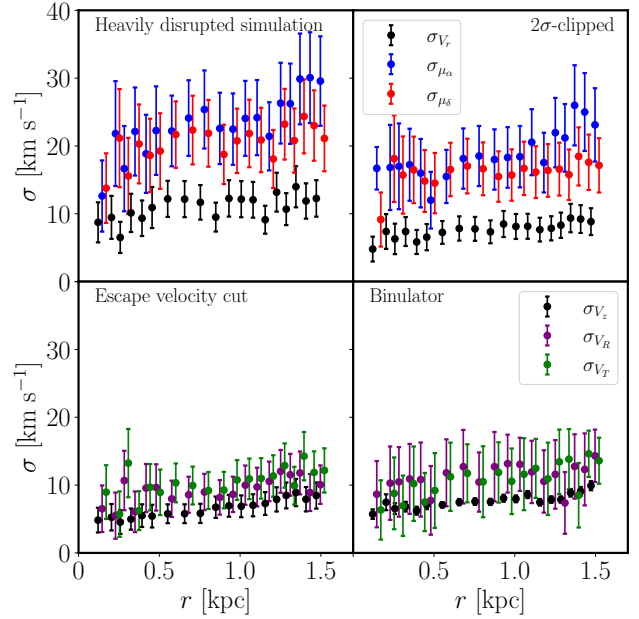


Figure 6. Velocity dispersion profiles for the inner regions of the heavily disrupted simulation. The black points show the velocity dispersion along the line-of-sight (σ_{V_r} in the top panels, σ_{V_z} in the bottom panels), the blue points σ_{μ_α} , the red points σ_{μ_δ} , the purple points σ_{V_R} , and the dark green points σ_{V_T} . *Top left panel:* velocity dispersions for the full data sample. *Top right panel:* Velocity dispersions after 2σ -clipping the velocity distributions, which are assumed to be Gaussians (see Fig. 1). *Bottom left panel:* velocity dispersions after iterated escape velocity cuts. *Bottom right panel:* velocity dispersions after the decontamination done by the BINULATOR. Inside each panel the bins are the same but are displaced artificially along the X-axis for clarity.

profiles recovered by our models are reported in Appendix A for completeness.

4.2.1 Removing tidal debris

We first check the impact of the removal of tidal debris by the BINULATOR. Fig. 8 compares the dispersions of the data processed by the BINULATOR (right) with the dispersion profiles of the observed data, taken as simple variances of each data bin (left). The decontamination has dampened the tangential anisotropy, with only some mild residual contamination likely due to the physical onset of tides (Read et al. 2006b) remaining after $r = 1.5$ kpc, this is reminiscent of the behaviour of the heavily disrupted mock in Fig. 6 and it is the reason why we limited the GRAVSPHERE fitting to within the half-mass radius.

4.2.2 The GRAVSPHERE model of the SMC

In Fig. 9, we show the GRAVSPHERE recovery of the dark matter density (left) and velocity anisotropy (right) profiles for the real SMC. As reflected in the data (Fig. 8), GRAVSPHERE favours some mild tangential anisotropy, though at 95% confidence it is consistent with being isotropic at all radii probed. The density profile is well-constrained over the range $0.5 \lesssim R/R_{1/2} \lesssim 2$ and appears more cusp-like than cored (constant density). We discuss this further in §4.2.4.

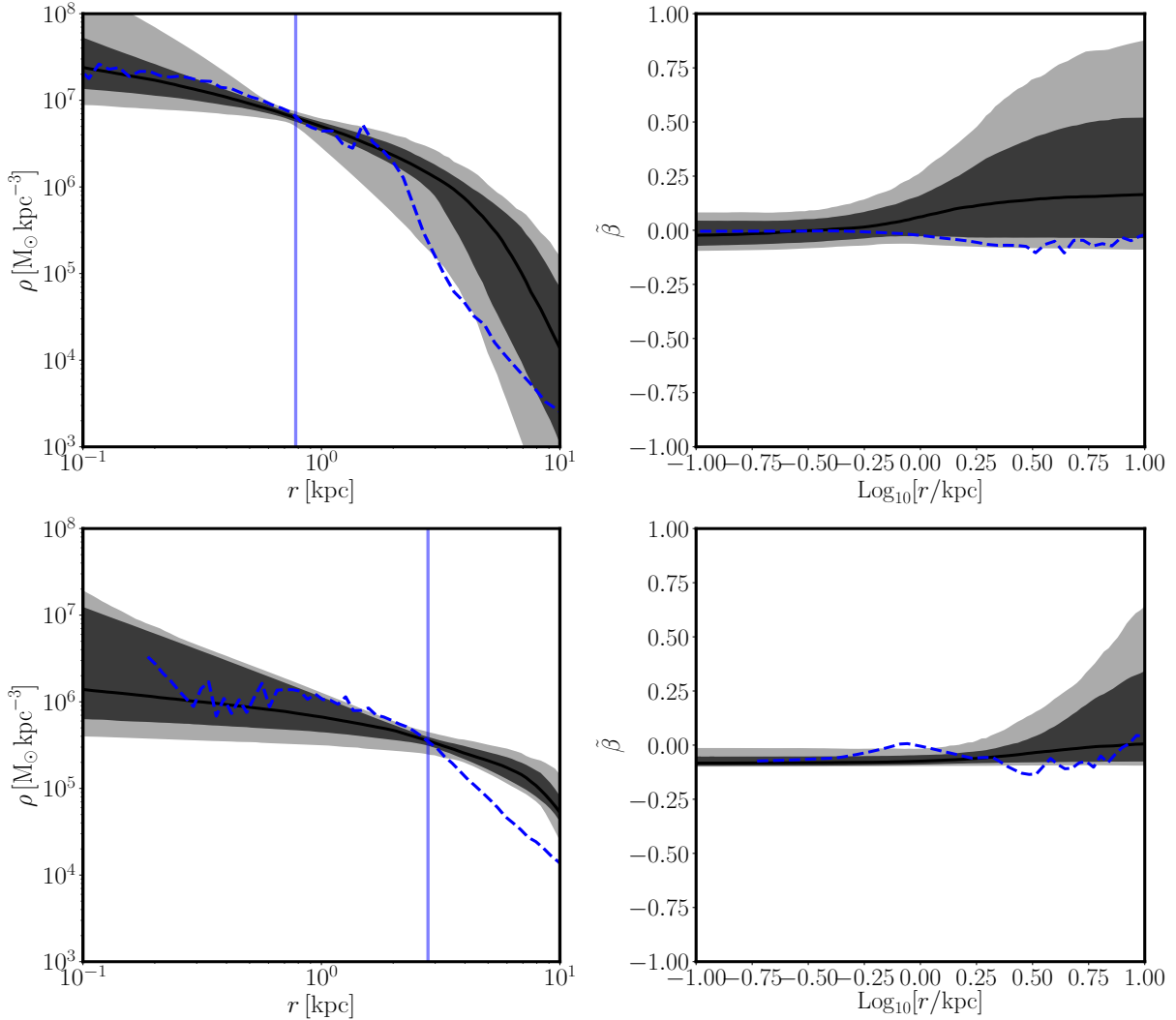


Figure 7. *Left panels:* recovered mass density profile, $\rho(r)$, of the bound (top) and heavily disrupted (bottom) simulations. The black lines and grey contours mark the median, 68% (dark grey), and 95% (light grey) confidence intervals of the GRAVSPHERE fit, respectively. The blue dashed lines show the profiles computed from the simulation data. The blue vertical lines mark the half-stellar mass radius computed by BINULATOR. *Right panels:* recovered symmetrised anisotropy profile $\tilde{\beta}(r)$ for the bound (top) and heavily disrupted (bottom) simulations. The solid black lines, grey contours, vertical blue lines, and blue dashed lines are as in the left panels.

4.2.3 The present and pre-infall mass of the SMC

Regarding the mass of the SMC, the recovered density profile suggests a dark matter mass within 3 kpc of $M_{DM}(\leq 3 \text{ kpc}) = 1.39 \pm 0.08 \times 10^9 M_{\odot}$ and a stellar mass within the same radius of $M_{*}(\leq 3 \text{ kpc}) = 0.34 \pm 0.05 \times 10^9 M_{\odot}$. We compare this with other literature estimates in §5.2.

GRAVSPHERE also provides us with constraints on the halo virial mass, $M_{200} = 2.61^{+1.95}_{-1.16} \times 10^{10} M_{\odot}$ (see Fig. 10), and concentration parameter, $c_{200} = 16.58 \pm 11.27$.

Given the extensive tidal disruption experienced by the SMC, it is not entirely clear how we should interpret the recovered M_{200} from present-day dynamical tracers. GRAVSPHERE does attempt to model the impact of tidal stripping through the tidal radius and density fall off model parameters, r_t and δ (see §3 and Equation 9). Unfortunately, we could not obtain constraints on r_t and δ that are bound only by our priors. Furthermore, GRAVSPHERE is not able to account for historic mass loss from inside r_t , neither from tidal stripping nor tidal shocks (e.g. Read et al. 2006b). As such, any

estimate of M_{200} will be a *lower bound* on the SMC’s pre-infall halo mass.

Despite the above caveats, GRAVSPHERE yields an estimate of the SMC’s pre-infall M_{200} that overlaps, within our 95% confidence intervals, with that obtained from abundance matching (e.g. Read & Erkal 2019): $M_{200, \text{abund}} = 7.73 \pm 1.69 \times 10^{10} M_{\odot}$ (see the solid and dashed red lines in Fig. 10 that mark the median and $\pm 68\%$ confidence intervals of $M_{200, \text{abund}}$).

Considering the, likely more robust, pre-infall $M_{200, \text{abund}}$ estimation, our recovered c_{200} parameter is consistent (within the 68% uncertainty) with the value expected in Λ CDM (~ 11 from Dutton & Macciò 2014) for a galaxy of the halo mass of the pre-infall SMC.

4.2.4 The inner dark matter density of the SMC: testing dark matter heating models

Armed with our recovered dark matter density profile and M_{200} for the SMC, we now turn to its position in the ρ_{DM} - M_{200} plane. As

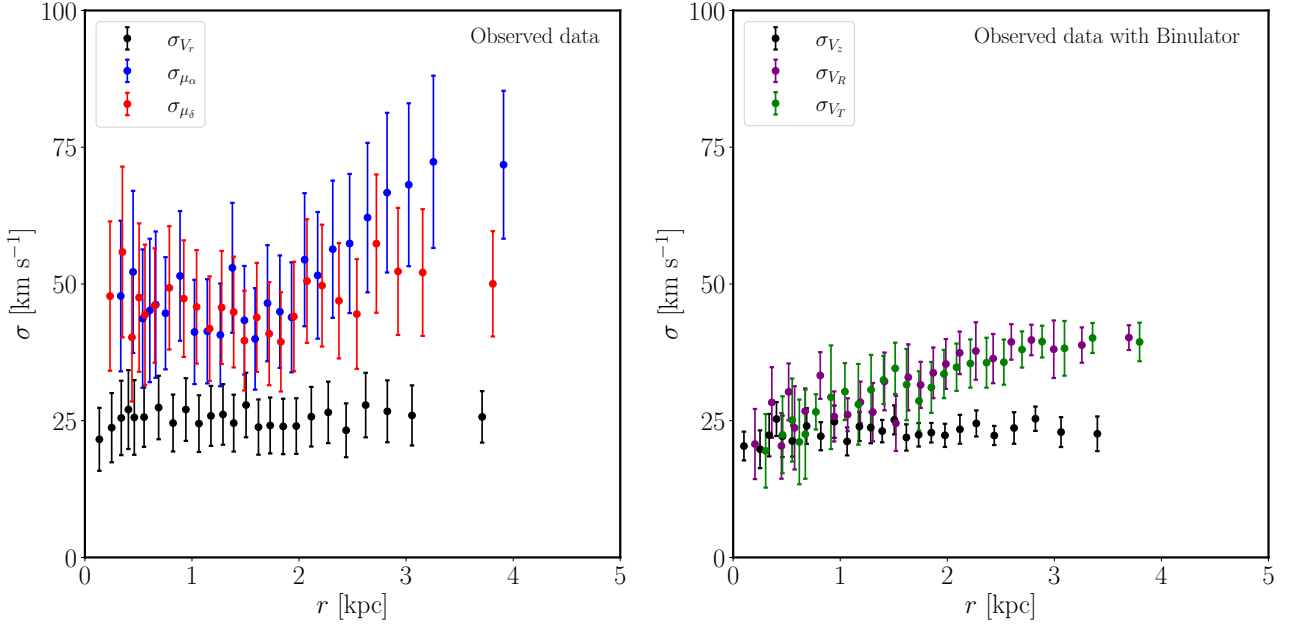


Figure 8. *Left panel:* dispersion profiles of V_r (black points), μ_α (blue points), and μ_δ (red points) for the observed data. The data are binned at the same positions but displaced along the X-axis for clarity. *Right panel:* dispersion profiles of V_z (black points), V_R (purple points), and V_T (dark green points) for the observed data after the BINULATOR fit of the velocity distributions. The data are binned at the same positions but displaced along the X-axis for clarity. The rising anisotropy after ~ 1.5 kpc likely owes to the physical onset of tides, rather than artificial inflation of the dispersions due to line-of-sight contamination. As such, BINULATOR is unable to correct for this. For this reason, we limit our fits to within the half-mass radius.

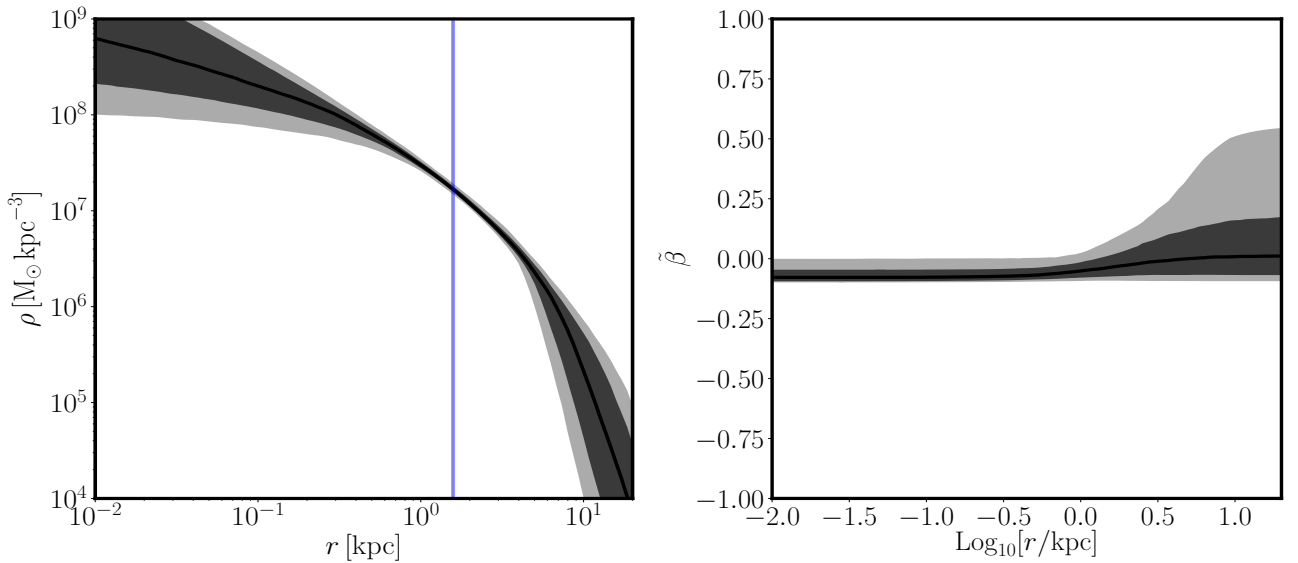


Figure 9. *Left panel:* $\rho(r)$ profile recovered by GRAVSPHERE for the SMC data. The black line is the best-fit solution and the dark and light gray regions are, respectively, the 68% and 95% confidence intervals. The faint blue vertical line is the recovered half-light radius. *Right panel:* $\tilde{\beta}(r)$ profile recovered by GRAVSPHERE for the SMC data. The black line is the best-fit solution and the dark and light gray regions are, respectively, the 68% and 95% confidence intervals.

first proposed in Read et al. (2019) (and see also §1), this provides a key test of “dark matter heating” models. For M_{200} , we will use the abundance matching pre-infall halo mass for the SMC: $M_{200,\text{abund}} = 7.73 \pm 1.69 \times 10^{10} M_\odot$ (Read & Erkal 2019). As discussed above, this is likely to be a more reliable estimate than that based on the SMC’s current dynamical state.

Fig. 11 compares the theoretical expectations for perfectly pre-

served dark matter cusps in a Λ CDM cosmology (gray bands) and complete cusp-core transformations due to dark matter heating (light blue bands) with the data from (Read et al. 2019) (black, blue and purple circles) and the SMC (red square). The left panel shows estimates of the dark matter density at 150 pc from the centres of the galaxies; the right panel at 500 pc. The black symbols are galaxies that stopped forming stars more than 6 Gyrs ago, the purple

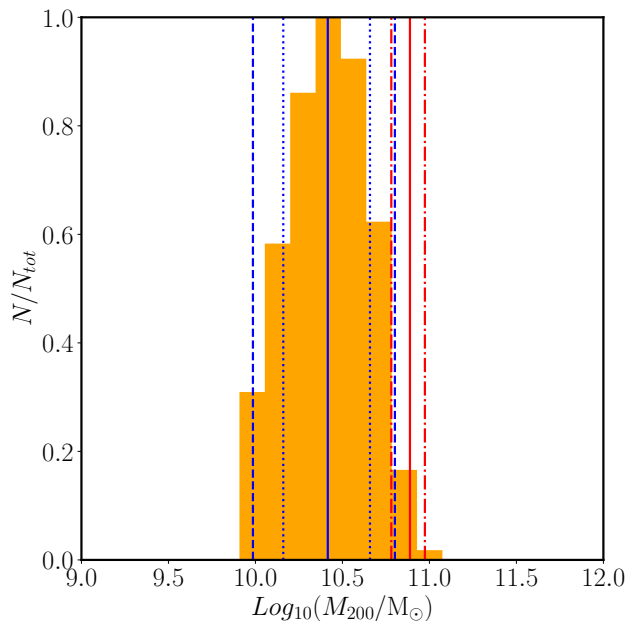


Figure 10. Distribution of the M_{200} values recovered by GRAVSPHERE (orange histogram). The mean value of the distribution is marked by the solid blue line, the dotted blue lines denote the 68% confidence interval while the dashed blue lines indicate the 95% confidence interval. The value reported by Read & Erkal (2019) is marked by a solid red line with its 68% confidence interval denoted by the dot-dashed red lines.

symbol is a galaxy that stopped forming stars 3 – 6 Gyrs ago and the blue symbols are galaxies that stopped forming stars in the last 3 Gyrs. All galaxies have been selected to be tidally isolated today (see Read et al. 2019).

Firstly, notice that at low M_{200} the blue and black bands overlap. This is because the dark matter core size scales with $\sim R_{1/2}$ which in turn correlates with M_{200} . As M_{200} is reduced, the expected core size shrinks and at a fixed length scale, the cusped and cored models begin to overlap. This happens at even higher mass for the $\rho_{\text{DM}}(500 \text{ pc})$ plot (right panel). Secondly, notice that the black and purple data points, corresponding to galaxies whose star formation shut down long ago, are consistent with dense dark matter cusps. By contrast, those dwarfs with recent star formation (blue data points) have had the most dark matter heating and are consistent with fully formed dark matter cores. The SMC, however, (red data point) has a much higher pre-infall M_{200} than any of the data points taken from Read et al. (2019); at 150 pc (left panel) it has a central density consistent with a dark matter cusp, albeit with large errors. At 500 pc (right panel), despite the model being better-constrained (lower errors), it is not able to distinguish between a cusp or a core and both are, ever so slightly, consistent within the errors. The SMC conserving its dark matter cusp is in line with the evidence of cusps being resilient to tides (Errani & Peñarrubia 2020; Errani et al. 2023).

We now consider whether the above behaviour – galaxies moving from being cusped to cored and then back to cusped again – is consistent with dark matter heating models. To test this, we switch from the $\rho_{\text{DM}}-M_{200}$ plane to the $\rho_{\text{DM}}-M_*/M_{200}$ plane. As discussed in §1, M_*/M_{200} – to leading order – indicates how much energy is available to drive dark matter heating (e.g. Peñarrubia et al. 2012). We expect dark matter heating to increase with increasing M_*/M_{200} until the self-gravity of the stars begins to dominate over

the dark matter at which point dark matter heating becomes inefficient again (e.g. Di Cintio et al. 2014a). In Fig. 12, we combine our data for the SMC with literature data from Read et al. 2019, Bouché et al. 2022 (courtesy of N. F. Bouché) and Cooke et al. 2022 (courtesy of R. C. Levy) to explicitly test this. We can see from Fig. 12 the relationship between central dark matter density at 150 pc and the stellar-to-halo mass ratio, M_*/M_{200} , for the data (squares and stars) as compared to several different models (coloured lines). The colours denote tracks of constant M_{200} , as marked by the colour-bars. The data points are coloured similarly by their median M_{200} , as estimated from abundance matching. The top left panel of Fig. 12 shows a classical NFW model (Navarro et al. 1996b) without dark matter heating. This model fits the more dense ‘cusp’-like dwarfs, but fails to reproduce the lower density ‘core’-like dwarfs in the range: $5 \times 10^{-4} \lesssim M_*/M_{200} \lesssim 10^{-2}$. The top right panel of Fig. 12 shows the Di Cintio et al. (2014b) model which correctly reproduces the qualitative behaviour seen in the data, with cusp-like densities below $M_*/M_{200} \lesssim 5 \times 10^{-4}$, core-like densities in the range $5 \times 10^{-4} \lesssim M_*/M_{200} \lesssim 5 \times 10^{-3}$ and cusp-like densities again for $M_*/M_{200} \gtrsim 5 \times 10^{-3}$. However, there are quantitative differences, with the model favouring a slower and smoother transition between the cusped and cored regimes (and back again) as compared to the data (for example, cusp-like densities at $M_*/M_{200} \sim 5 \times 10^{-4}$ are not expected by the model). We must note that the model has been computed assuming the median concentration parameter, c_{200} , in a Λ CDM cosmology (Dutton & Macciò 2014). This may not be appropriate for the dwarf spheroidal satellites of the Milky Way that likely fell in long ago (Read & Erkal 2019) and may, therefore, be biased to higher concentration parameters (e.g. Springel et al. 2008). In Appendix C we explore the effect of the introduction of a $2 - \sigma$ bias above the median in the estimation of the concentration parameter of dark matter halos, c_{200} . Including this bias, the model does pass comfortably through the data points for the high central density dwarf spheroidals at low and high M_*/M_{200} (including the SMC). Whether this is the correct interpretation of the behaviour of these data, or whether the dark matter heating model of Di Cintio et al. (2014a) is not quite correct, remains to be seen.

The bottom left panel of Fig. 12 shows the Lazar et al. (2020) model which correctly reproduces the behaviour seen in the data up until $M_*/M_{200} \sim 10^{-2}$, but fails to account for the more dense halos at higher mass ratios. The errors for most of these higher mass ratio data points remain large, but the data point we derive here for the SMC certainly seems to be in significant tension with the predictions from Lazar et al. (2020). This highlights two important points: (i) not all dark matter heating models in the literature make the same predictions, and (ii) the latest data are now able to quantitatively test these models.

Finally, in the bottom right panel of Fig. 12 we show a handy analytic function, built on the CORENFW profile (equation 11), that captures the main features of the data. This introduces an M_*/M_{200} dependence on the n parameter (that determines how cusped or cored the profile is):

$$n = \kappa_3 \exp\left(\frac{-(\text{Log}_{10}(M_*/M_{200}) - \kappa_1)^2}{\kappa_2}\right) \quad (24)$$

where $\kappa_1 = -2.75$, $\kappa_2 = 0.2$ and $\kappa_3 = 1.25$. Readers may find this useful as a compact analytic description of the behaviour of the data and/or to test their own favoured models.

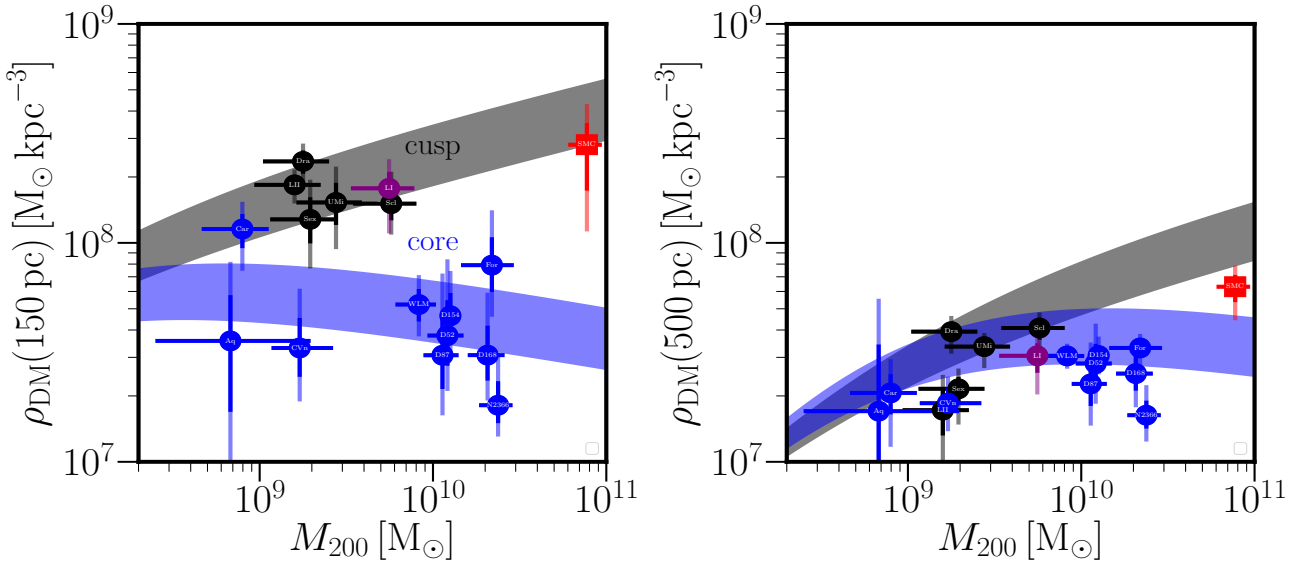


Figure 11. *Left panel:* Inner dark matter density (at 150pc) as a function of halo mass for a sample of dwarf galaxies. The gray band marks the theoretical expectation for perfectly preserved cusps (no dark matter heating) while the light blue band denotes the expectation for complete core transformation (maximal dark matter heating). The black symbols are dwarf galaxies that stopped forming stars more than 6 Gyrs ago, the purple symbol is a galaxy that stopped forming stars between 6 and 3 Gyrs ago, the blue symbols are galaxies that stopped forming stars in the last 3 Gyrs and the red square is the SMC. The error bars for the symbols are fully coloured for the 1σ value and faintly coloured up to the 2σ value. *Right panel:* same as the left panel but for the density estimated at 500pc (instead of 150pc).

4.2.5 The astrophysical J -factor and D -factor of the SMC

Given their dense environments, dwarf galaxies can be suitable candidates for searches of dark matter annihilation and/or decay events (Kuhlen 2010) so we will conclude this section with a look at the SMC in this context. The density estimation of GRAVSPHERE can be used to derive the J -factor: the integral of the square of the dark matter density along the line-of-sight and over a solid angle $\delta\Omega$ (Alvarez et al. 2020). This parameter quantifies the dependence of dark matter annihilation searches on the density of the astrophysical target being searched. We recovered the distribution of J -factors for the SMC, shown in Fig. 13. This has a mean of $18.99 \pm 0.16 \text{ GeV}^2 \text{ cm}^{-5}$, shown as the solid red line in the figure. We also recovered the distribution of the D -factor: the integral of the dark matter density along the line-of-sight and over a solid angle $\delta\Omega$ (Alvarez et al. 2020). This is the relevant quantity for testing decaying dark matter models. We find a mean value of $18.73 \pm 0.04 \text{ GeV}^2 \text{ cm}^{-5}$. Both the J - and D -factor are interestingly competitive with the densest dwarf spheroidals known to date around the Milky Way (e.g. Alvarez et al. 2020), suggesting that the SMC is a prime target for such annihilation and decay searches. While the SMC has a much stronger gamma-ray background than other nearby gas-free dwarf spheroidal galaxies (like Draco), this background can be well-modelled using the observed distribution of stellar light, gas and high energy point sources, yielding competitive constraints on dark matter models (i.e. Caputo et al. 2016).

5 DISCUSSION

5.1 The impact of priors

Before delving deeper into the information that can be extracted from the mass model of the SMC, it is worth discussing briefly the choices of priors operated throughout the modeling process and

how they affect the results. The flat priors assumed for the mass profile (rows 1 to 6 in Tab. 1) were purposefully weak to allow for the recovery of any kind of final model (be it cuspy or cored). The M_{200} and c_{200} bounds were informed by previous studies of the SMC (respectively Read & Erkal 2019 and Besla et al. 2012) while the others were left wide to allow for any possible solution. The priors assumed for the velocity PDFs recovered by the BINULATOR (rows 13 to 15 of Tab. 1) were informed by our previous study of the SMC bulk motion (De Leo et al. 2020), based on the same observational data. For the proper decontamination of the debris it was also fundamental to allow the BINULATOR to use at least two secondary Gaussians (priors on rows 16 to 21 of Tab. 1) to fit for contaminants on either side of the SMC bulk velocity distribution. As for the priors on the mass profile, we favoured weaker priors for the anisotropy parameters (rows 9 to 12 of Tab. 1). We found that tighter priors (i.e. $-0.01 \leq \beta_0 \leq 0.01$) produced a slightly more cored density profile at the expense of strongly enforcing a zero value of the central anisotropy profile (see Fig. B1 in Appendix B).

5.2 The present-day mass of the SMC

It is difficult to make a proper comparison of our recovered present-day mass of the SMC with values in the literature as most estimations were derived from mass models that assumed gas and stars were bound by the SMC potential to large radii. We obtain $M_{DM}(\leq 3 \text{ kpc}) = 1.39^{+0.08}_{-0.07} \times 10^9 M_\odot$ and $M_*(\leq 3 \text{ kpc}) = 0.34 \pm 0.05 \times 10^9 M_\odot$ (§4.2.3). Summing to this the total gas mass measured within the same radius ($5.6 \times 10^8 M_\odot$; Stanimirović et al. 1999; Stanimirović et al. 2004; Brüns et al. 2005), we obtain a total present-day mass of the SMC equal to $M_{\text{tot}}(\leq 3 \text{ kpc}) = 2.29 \pm 0.46 \times 10^9 M_\odot$. While this value is consistent with the estimate for total SMC mass of $2.4 \times 10^9 M_\odot$ in Stanimirović et al. (2004), the underlying assumptions of our methods are quite different (the model in Stanimirović et al. 2004 was a two-component model

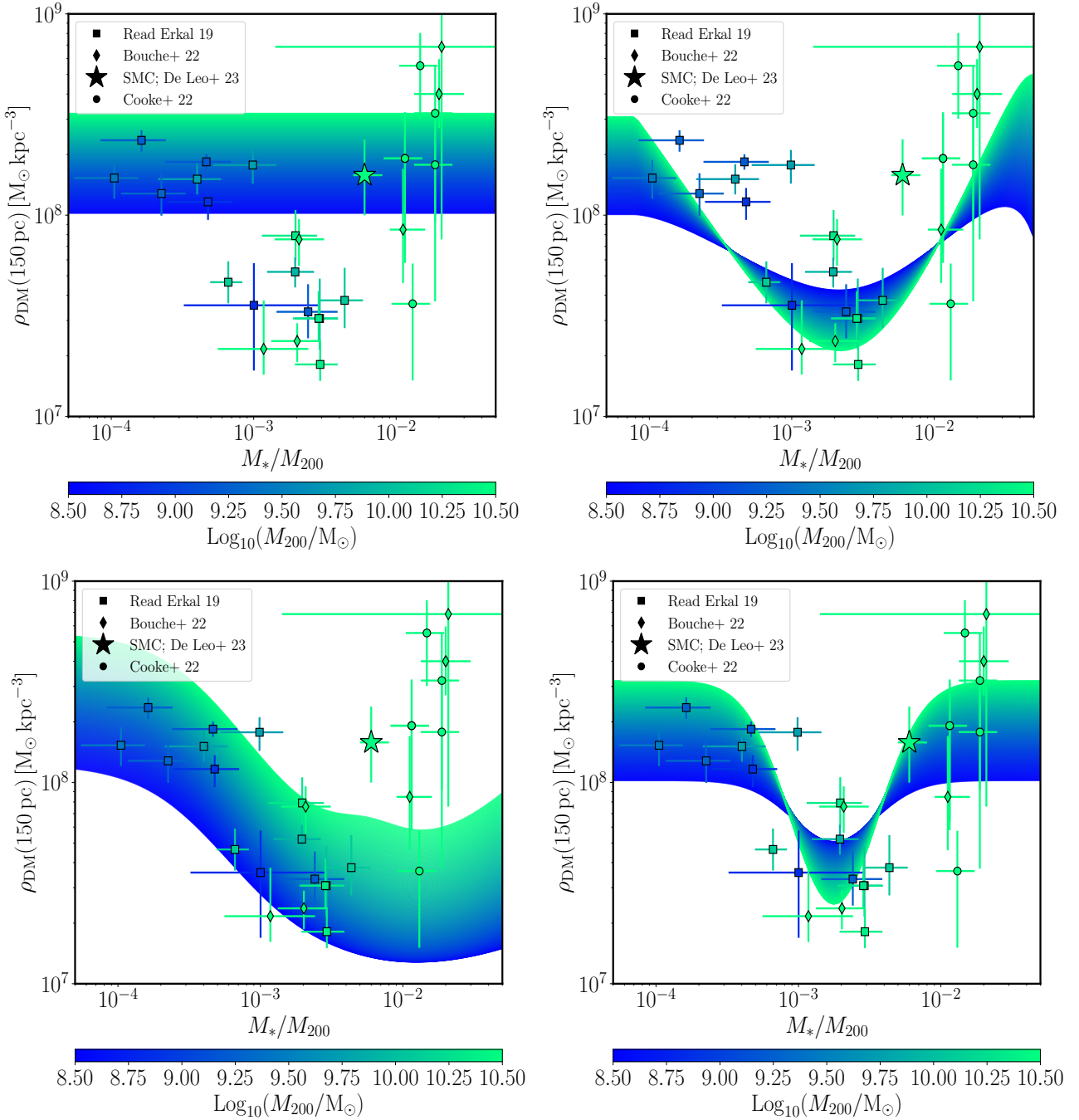


Figure 12. Central dark matter density ρ_{DM} at 150 pc from the galactic centre against stellar-to-halo mass ratio M_*/M_{200} for the data presented in [Read & Erkal \(2019\)](#), [Bouché et al. \(2022\)](#), [Cooke et al. \(2022\)](#) and the SMC (the coloured symbols) compared to different dark matter models (coloured bands). In all panels, the colour of the points and of specific positions along the bands marks the pre-infall halo mass, M_{200} (see the colourbar). *Top left panel:* the band is the prediction of the [Navarro et al. \(1996b\)](#) model. *Top right panel:* the band is the prediction of the [Di Cintio et al. \(2014b\)](#) model. *Bottom left panel:* the band is the prediction of the [Lazar et al. \(2020\)](#) model. *Bottom right panel:* The band is a modified coreNFW model tuned to the data.

without dark matter) so it is challenging to meaningfully compare the two values. Our total mass is also consistent with the lower bound of the estimation from [Harris & Zaritsky \(2006\)](#), who derived a total mass between $2.7 \times 10^9 M_{\odot}$ and $5.1 \times 10^9 M_{\odot}$ through a simple virial analysis based on stellar kinematics. The smaller value that we recover is due to the fact our model excludes the stars in the tidal debris from the computation of the bound SMC mass.

5.3 Comparison with dark matter annihilation literature

Our recovered value for the J -factor ($18.99 \pm 0.16 \text{ GeV}^2 \text{ cm}^{-5}$) is in good agreement with the estimate of [Caputo et al. \(2016\)](#) and – interestingly – on par with the isolated dwarf galaxy Draco ($18.69 \pm 0.05 \text{ GeV}^2 \text{ cm}^{-5}$ estimated in [Alvarez et al. \(2020\)](#)). The estimated D -factor ($18.73 \pm 0.04 \text{ GeV}^2 \text{ cm}^{-5}$) likewise is consistent with estimations for isolated dwarf galaxies (Draco, Tucana II estimated

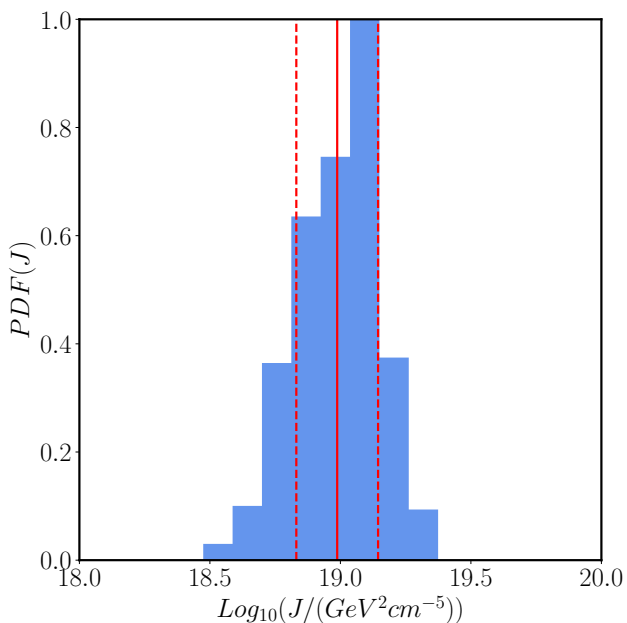


Figure 13. The PDF for the J -factor recovered by GRAVSPHERE (blue histogram). The mean value of the distribution is marked as a solid red line with dashed red lines marking the 68% confidence interval.

in Evans et al. 2016). This suggests that the SMC is a competitive target for the observation of gamma-rays and/or X-rays originating from dark matter annihilation and/or decay events, provided that its gamma-ray background is correctly modelled.

6 CONCLUSIONS

Using mock data we showed that, despite being subjected to heavy tidal disruption, the SMC can still be mass modelled with methods that require dynamical equilibrium. For this, we assumed that the galaxy is composed of a central bound remnant surrounded by tidal debris (as supported by the latest observational data, e.g. Graczyk et al. 2020). Given that building an unbiased mass model requires careful removal of tidal debris along the line-of-sight, we introduced the BINULATOR. We showed that this new method to achieve the decontamination successfully worked on mock data for a tidally disrupting SMC.

We then proceeded to apply a Jeans mass modelling method (BINULATOR+GRAVSPHERE) to ~ 6000 RGB stars with spectroscopic and proper motion data from *Gaia* EDR3 to build a new mass model of the SMC. The data decontamination employed by the BINULATOR and the use of the full dynamical information (the line-of-sight velocity distribution and proper motions) by GRAVSPHERE were instrumental in recovering a robust model which we could use to further explore the characteristics of the dark matter halo of the SMC. After the removal of the tidally unbound interlopers, we recovered both the mass density and the stellar velocity anisotropy profile (which shows the remaining stars to be isotropic at all radii within the uncertainties).

We provided a new estimate for the total present-day mass of the SMC, $M_{\text{tot}}(\leq 3 \text{ kpc}) = 2.29 \pm 0.46 \times 10^9 M_{\odot}$, based on stellar kinematics, which takes into account the extensive tidal disruption undergone by the galaxy.

Our model found that the SMC has a high central density,

$\rho_{\text{DM}}(150 \text{ pc}) = 1.58^{+0.80}_{-0.58} \times 10^8 M_{\odot} \text{ kpc}^{-3}$, which is consistent with a dark matter cusp within the Λ CDM paradigm. The inferred dark matter density profile provides an observational reference point for the halo mass scale at which dark matter heating becomes inefficient and is no longer able to drive a cusp-core transformation.

We used the SMC, together with previously available data, to test dark matter heating models in the literature, finding good qualitative agreement with the Di Cintio et al. (2014a) model but poorer agreement with the Lazar et al. (2020) model at $M_*/M_{200} > 10^{-2}$. We also introduced a new analytic density profile that gives a good fit to the central dark matter density of dwarf galaxies and its dependence on M_*/M_{200} .

Finally, from the recovered cuspy dark matter density profile, we derived an astrophysical J -factor of $18.99 \pm 0.16 \text{ GeV}^2 \text{ cm}^{-5}$ (D -factor of $18.73 \pm 0.04 \text{ GeV}^2 \text{ cm}^{-5}$), suggesting that the SMC is a very promising target for dark matter annihilation and decay searches.

ACKNOWLEDGEMENTS

The authors thank the anonymous referee for their insightful comments that improved the paper. MDL thanks Alessia Gualandris, Jorge Peñarrubia and Alex Drlica-Wagner for insightful comments and discussions which helped improve the present work. MDL also thanks Nicolas F. Bouché and Rebecca C. Levy for providing access to their data. The research leading to these results has received funding from the European Community’s Seventh Framework Programme (FP7/2013-2016) under grant agreement number 312430 (OPTICON). This work was also funded by ANID, Millenium Science Initiative, ICN12_009.

Software: this research made use of the Astropy (Astropy Collaboration et al. 2013, 2018), Healpy (Górski et al. 2005; Zonca et al. 2019), Matplotlib (Hunter 2007) and Numpy (Harris et al. 2020) packages.

DATA AVAILABILITY STATEMENT

The data underlying this article will be shared on reasonable request to the corresponding author.

REFERENCES

- Allende Prieto C., Koesterke L., Hubeiy I., Bautista M. A., Barklem P. S., Nahar S. N., 2018, *A&A*, **618**, A25
- Alvarez A., Calore F., Genina A., Read J., Serpico P. D., Zaldivar B., 2020, *J. Cosmology Astropart. Phys.*, **2020**, 004
- Astropy Collaboration et al., 2013, *A&A*, **558**, A33
- Astropy Collaboration et al., 2018, *AJ*, **156**, 123
- Avila-Reese V., Colín P., Valenzuela O., D’Onghia E., Firmani C., 2001, *ApJ*, **559**, 516
- Baes M., van Hese E., 2007, *A&A*, **471**, 419
- Besla G., Kallivayalil N., Hernquist L., van der Marel R. P., Cox T. J., Kereš D., 2012, *MNRAS*, **421**, 2109
- Bianchini P., van der Marel R. P., del Pino A., Watkins L. L., Bellini A., Fardal M. A., Libralato M., Sills A., 2018, *MNRAS*, **481**, 2125
- Binney J., 1980, *MNRAS*, **190**, 873
- Binney J., Mamon G. A., 1982, *MNRAS*, **200**, 361
- Binney J., Tremaine S., 2008, *Galactic dynamics*. Princeton, NJ: Princeton University Press, 2008
- Bode P., Ostriker J. P., Turok N., 2001, *ApJ*, **556**, 93
- Bouché N. F., et al., 2022, *A&A*, **658**, A76

- Bovy J., 2015, *ApJS*, 216, 29
- Bruderer C., Read J. I., Coles J. P., Leier D., Falco E. E., Ferreras I., Saha P., 2016, *MNRAS*, 456, 870
- Brüns C., et al., 2005, *A&A*, 432, 45
- Caputo R., Buckley M. R., Martin P., Charles E., Brooks A. M., Drlica-Wagner A., Gaskins J., Wood M., 2016, *Phys. Rev. D*, 93, 062004
- Carrera R., Conn B. C., Noël N. E. D., Read J. I., López Sánchez Á. R., 2017, *MNRAS*, 471, 4571
- Collins M. L. M., Read J. I., 2022, *Nature Astronomy*, 6, 647
- Collins M. L. M., et al., 2021, *MNRAS*, 505, 5686
- Cooke L. H., et al., 2022, *MNRAS*, 512, 1012
- De Leo M., Carrera R., Noël N. E. D., Read J. I., Erkal D., Gallart C., 2020, *MNRAS*, 495, 98
- Di Cintio A., Brook C. B., Macciò A. V., Stinson G. S., Knebe A., Dutton A. A., Wadsley J., 2014a, *MNRAS*, 437, 415
- Di Cintio A., Brook C. B., Dutton A. A., Macciò A. V., Stinson G. S., Knebe A., 2014b, *MNRAS*, 441, 2986
- Dobbie P. D., Cole A. A., Subramaniam A., Keller S., 2014, *MNRAS*, 442, 1663
- Dubinski J., Carlberg R. G., 1991, *ApJ*, 378, 496
- Dutton A. A., Macciò A. V., 2014, *MNRAS*, 441, 3359
- El-Badry K., Wetzel A., Geha M., Hopkins P. F., Kereš D., Chan T. K., Faucher-Giguère C.-A., 2016, *ApJ*, 820, 131
- El-Zant A., Shlosman I., Hoffman Y., 2001, *ApJ*, 560, 636
- Emami N., Siana B., Weisz D. R., Johnson B. D., Ma X., El-Badry K., 2019, *ApJ*, 881, 71
- Erkal D., et al., 2019, *MNRAS*, 487, 2685
- Errani R., Peñarrubia J., 2020, *MNRAS*, 491, 4591
- Errani R., Navarro J. F., Peñarrubia J., Famaey B., Ibata R., 2023, *MNRAS*, 519, 384
- Evans C. J., Howarth I. D., 2008, *MNRAS*, 386, 826
- Evans N. W., Sanders J. L., Geringer-Sameth A., 2016, *Phys. Rev. D*, 93, 103512
- Flores R. A., Primack J. R., 1994, *ApJ*, 427, L1
- Foreman-Mackey D., Hogg D. W., Lang D., Goodman J., 2013, *PASP*, 125, 306
- Gaia Collaboration et al., 2018, *A&A*, 616, A1
- Gaia Collaboration et al., 2021, *A&A*, 649, A1
- Genina A., et al., 2018, *MNRAS*, 474, 1398
- Genina A., et al., 2020, *MNRAS*, 498, 144
- Gnedin O. Y., Zhao H., 2002, *MNRAS*, 333, 299
- Górski K. M., Hivon E., Banday A. J., Wandelt B. D., Hansen F. K., Reinecke M., Bartelmann M., 2005, *ApJ*, 622, 759
- Graczyk D., et al., 2020, *ApJ*, 904, 13
- Gregory A. L., et al., 2020, *MNRAS*, 496, 1092
- Harris J., Zaritsky D., 2006, *AJ*, 131, 2514
- Harris C. R., et al., 2020, *Nature*, 585, 357
- Hatzidimitriou D., Cannon R. D., Hawkins M. R. S., 1993, *MNRAS*, 261, 873
- Hogan C. J., Dalcanton J. J., 2000, *Phys. Rev. D*, 62, 063511
- Hunter J. D., 2007, *Computing in Science and Engineering*, 9, 90
- Jacyszyn-Dobrzeniecka A. M., et al., 2016, *Acta Astron.*, 66, 149
- Jacyszyn-Dobrzeniecka A. M., et al., 2017, *Acta Astron.*, 67, 1
- Jeans J. H., 1922, *MNRAS*, 82, 122
- Kauffmann G., 2014, *MNRAS*, 441, 2717
- Kazantzidis S., Łokas E. L., Mayer L., 2013, *ApJ*, 764, L29
- Klimentowski J., Łokas E. L., Kazantzidis S., Prada F., Mayer L., Mamon G. A., 2007, *MNRAS*, 378, 353
- Kuhlen M., 2010, *Advances in Astronomy*, 2010, 162083
- Lazar A., et al., 2020, *MNRAS*, 497, 2393
- Leaman R., et al., 2012, *ApJ*, 750, 33
- Lindgren L., et al., 2018, *A&A*, 616, A2
- Lindgren L., et al., 2021, *A&A*, 649, A2
- Mamon G. A., Łokas E. L., 2005, *MNRAS*, 363, 705
- Martizzi D., Teyssier R., Moore B., 2013, *MNRAS*, 432, 1947
- Mashchenko S., Wadsley J., Couchman H. M. P., 2008, *Science*, 319, 174
- Massana P., et al., 2020, *MNRAS*, 498, 1034
- McConnachie A. W., 2012, *AJ*, 144, 4
- Merrifield M. R., Kent S. M., 1990, *AJ*, 99, 1548
- Moore B., 1994, *Nature*, 370, 629
- Muraveva T., et al., 2018, *MNRAS*, 473, 3131
- Navarro J. F., Eke V. R., Frenk C. S., 1996a, *MNRAS*, 283, L72
- Navarro J. F., Frenk C. S., White S. D. M., 1996b, *ApJ*, 462, 563
- Navarro J. F., Frenk C. S., White S. D. M., 1997, *ApJ*, 490, 493
- Nidever D. L., et al., 2021, *AJ*, 161, 74
- Niederhofer F., et al., 2021, *MNRAS*, 502, 2859
- Noël N. E. D., Conn B. C., Carrera R., Read J. I., Rix H. W., Dolphin A., 2013, *ApJ*, 768, 109
- Noël N. E. D., Conn B. C., Read J. I., Carrera R., Dolphin A., Rix H. W., 2015, *MNRAS*, 452, 4222
- Oñorbe J., Boylan-Kolchin M., Bullock J. S., Hopkins P. F., Kereš D., Faucher-Giguère C.-A., Quataert E., Murray N., 2015, *MNRAS*, 454, 2092
- Olsen K. A. G., Zaritsky D., Blum R. D., Boyer M. L., Gordon K. D., 2011, *ApJ*, 737, 29
- Oman K. A., Marasco A., Navarro J. F., Frenk C. S., Schaye J., Benítez-Llambay A., 2019, *MNRAS*, 482, 821
- Orkney M. D. A., et al., 2021, *MNRAS*, 504, 3509
- Peñarrubia J., Pontzen A., Walker M. G., Koposov S. E., 2012, *ApJ*, 759, L42
- Plummer H. C., 1911, *MNRAS*, 71, 460
- Pontzen A., Governato F., 2012, *MNRAS*, 421, 3464
- Pontzen A., Governato F., 2014, *Nature*, 506, 171
- Read J. I., Erkal D., 2019, *MNRAS*, 487, 5799
- Read J. I., Gilmore G., 2005, *MNRAS*, 356, 107
- Read J. I., Steger P., 2017, *MNRAS*, 471, 4541
- Read J. I., Wilkinson M. I., Evans N. W., Gilmore G., Kleya J. T., 2006a, *MNRAS*, 366, 429
- Read J. I., Wilkinson M. I., Evans N. W., Gilmore G., Kleya J. T., 2006b, *MNRAS*, 367, 387
- Read J. I., Agertz O., Collins M. L. M., 2016a, *MNRAS*, 459, 2573
- Read J. I., Iorio G., Agertz O., Fraternali F., 2016b, *MNRAS*, 462, 3628
- Read J. I., Iorio G., Agertz O., Fraternali F., 2017, *MNRAS*, 467, 2019
- Read J. I., Walker M. G., Steger P., 2018, *MNRAS*, 481, 860
- Read J. I., Walker M. G., Steger P., 2019, *MNRAS*, 484, 1401
- Read J. I., et al., 2021, *MNRAS*, 501, 978
- Richardson T., Fairbairn M., 2014, *MNRAS*, 441, 1584
- Ripepi V., et al., 2014, *MNRAS*, 442, 1897
- Ripepi V., et al., 2017, *MNRAS*, 472, 808
- Rojas-Niño A., Read J. I., Aguilar L., Delorme M., 2016, *MNRAS*, 459, 3349
- Sanders J. L., Evans N. W., 2020, *MNRAS*, 499, 5806
- Schive H.-Y., Chiueh T., Broadhurst T., 2014, *Nature Physics*, 10, 496
- Scowcroft V., Freedman W. L., Madore B. F., Monson A., Persson S. E., Rich J., Seibert M., Rigby J. R., 2016, *ApJ*, 816, 49
- Sharp R., Birchall M. N., 2010, *Publ. Astron. Soc. Australia*, 27, 91
- Smith R., Choi H., Lee J., Rhee J., Sanchez-Janssen R., Yi S. K., 2016, *ApJ*, 833, 109
- Sparre M., Hayward C. C., Feldmann R., Faucher-Giguère C.-A., Muratov A. L., Kereš D., Hopkins P. F., 2017, *MNRAS*, 466, 88
- Spergel D. N., Steinhardt P. J., 2000, *Phys. Rev. Lett.*, 84, 3760
- Springel V., 2005, *MNRAS*, 364, 1105
- Springel V., et al., 2008, *MNRAS*, 391, 1685
- Stanimirović S., Staveley-Smith L., Dickey J. M., Sault R. J., Snowden S. L., 1999, *MNRAS*, 302, 417
- Stanimirović S., Staveley-Smith L., Jones P. A., 2004, *ApJ*, 604, 176
- Strigari L. E., Bullock J. S., Kaplinghat M., 2007, *ApJ*, 657, L1
- Teyssier R., Pontzen A., Dubois Y., Read J. I., 2013, *MNRAS*, 429, 3068
- Wilkinson M. I., Kleya J. T., Evans N. W., Gilmore G. F., Irwin M. J., Grebel E. K., 2004, *ApJ*, 611, L21
- Zhang H.-X., Hunter D. A., Elmegreen B. G., Gao Y., Schrubba A., 2012, *AJ*, 143, 47
- Zivick P., et al., 2018, *ApJ*, 864, 55
- Zivick P., et al., 2019, *ApJ*, 874, 78
- Zivick P., Kallivayalil N., van der Marel R. P., 2021, *ApJ*, 910, 36

Zonca A., Singer L., Lenz D., Reinecke M., Rosset C., Hivon E., Gorski K., 2019, *Journal of Open Source Software*, 4, 1298
 Zoutendijk S. L., et al., 2021a, arXiv e-prints, p. [arXiv:2112.09374](https://arxiv.org/abs/2112.09374)
 Zoutendijk S. L., Brinchmann J., Bouché N. F., den Brok M., Krajnović D., Kuijken K., Maseda M. V., Schaye J., 2021b, *A&A*, 651, A80
 van de Ven G., van den Bosch R. C. E., Verolme E. K., de Zeeuw P. T., 2006, *A&A*, 445, 513
 van der Marel R. P., 1994, *MNRAS*, 270, 271

APPENDIX A: GRAVSPHERE RECOVERED PROFILES

In this Appendix, we show the surface brightness profile and the three velocity profiles (line-of-sight, radial and tangential) recovered by GRAVSPHERE for the case of the heavily disrupted simulation (Fig. A1) and for the real SMC (Fig. A2). As can be seen in both cases, the LOS data provides most of the constraining power to the model.

APPENDIX B: DIFFERENT PRIORS

As discussed in the main text in Sec. 5.1, we tested the effect of different priors on our parameter recovery. Most of the tests (changing the bounds of the priors on n or restricting to smaller maximum r_c or r_t) had negligible impact on our models. The most impactful prior choice was on β_0 , specifically on enforcing a tighter prior with $-0.01 \leq \beta_0 \leq 0.01$. Even this change had only a minor impact on the recovered mass density profile, $\rho(r)$, as can be seen in Fig. B1. Notice that the density profile (left) now suggests a small inner core within the 95% confidence intervals. However, the best fit results are in good agreement with our default broader priors (see Figure 9) and still consistent with a dark matter cusp.

APPENDIX C: CONCENTRATION PARAMETER BIAS

In this Appendix we test whether a $2\text{-}\sigma$ bias in the estimation of the concentration parameter c_{200} can reconcile the Di Cintio et al. (2014b) model with the observational data. In Fig. C1 we show the model prediction for the median c_{200} on the left panel and the model prediction for concentration parameters $2\text{-}\sigma$ higher on the right panel. Notice how the higher density data (including the SMC) that were not fit well by the base model are now consistent with the predict curve of the right panel. This points to the fact that the discrepancy between the prediction of the Di Cintio et al. (2014b) model and the observational data has a magnitude comparable to the scatter in the c_{200} estimation. In other words, this means that the data are not necessarily inconsistent with the model and the SMC and other dwarfs might be interpreted as higher concentration halos.

This paper has been typeset from a $\text{\TeX}/\text{\LaTeX}$ file prepared by the author.

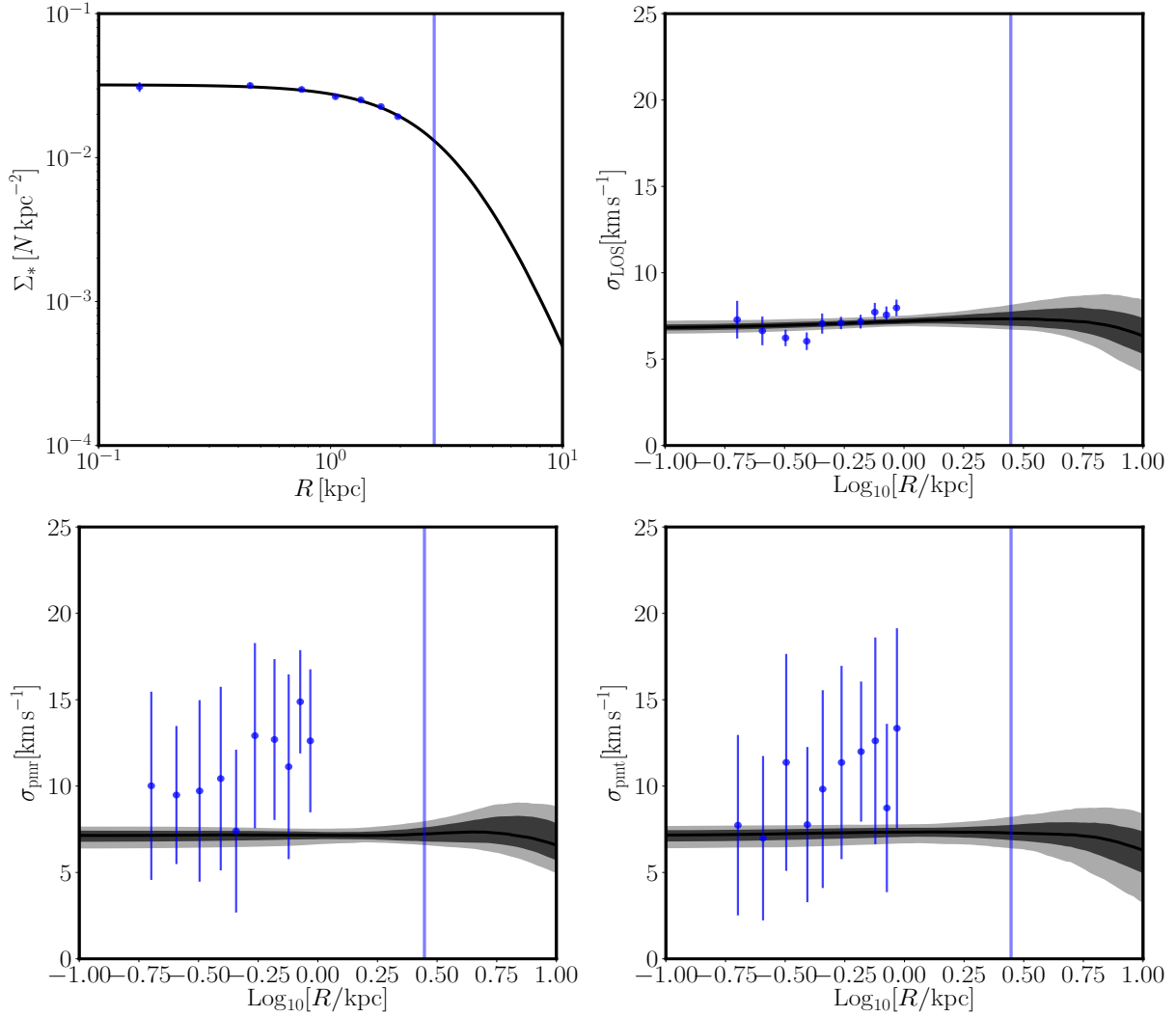


Figure A1. GRAVSPHERE recovered profiles for the heavily disrupted simulation. *Top left panel:* surface brightness $\Sigma_*(r)$. The black line is the GRAVSPHERE fit, the blue points are the simulation data and the faint blue line marks the half-light radius computed by GRAVSPHERE. *Top right panel:* velocity dispersion profile along the line of sight σ_{LOS} , the black line is GRAVSPHERE best fit solution, the dark and light grey contour are respectively the 68% and the 95% confidence intervals, the blue points with error bars are the binned data and the faint blue line marks the half-light radius computed by GRAVSPHERE. *Bottom left panel:* radial velocity dispersion profile σ_{rad} , lines and symbols are the same as for σ_{LOS} . *Bottom right panel:* tangential velocity dispersion profile σ_{tan} , lines and symbols are the same as for σ_{LOS} .

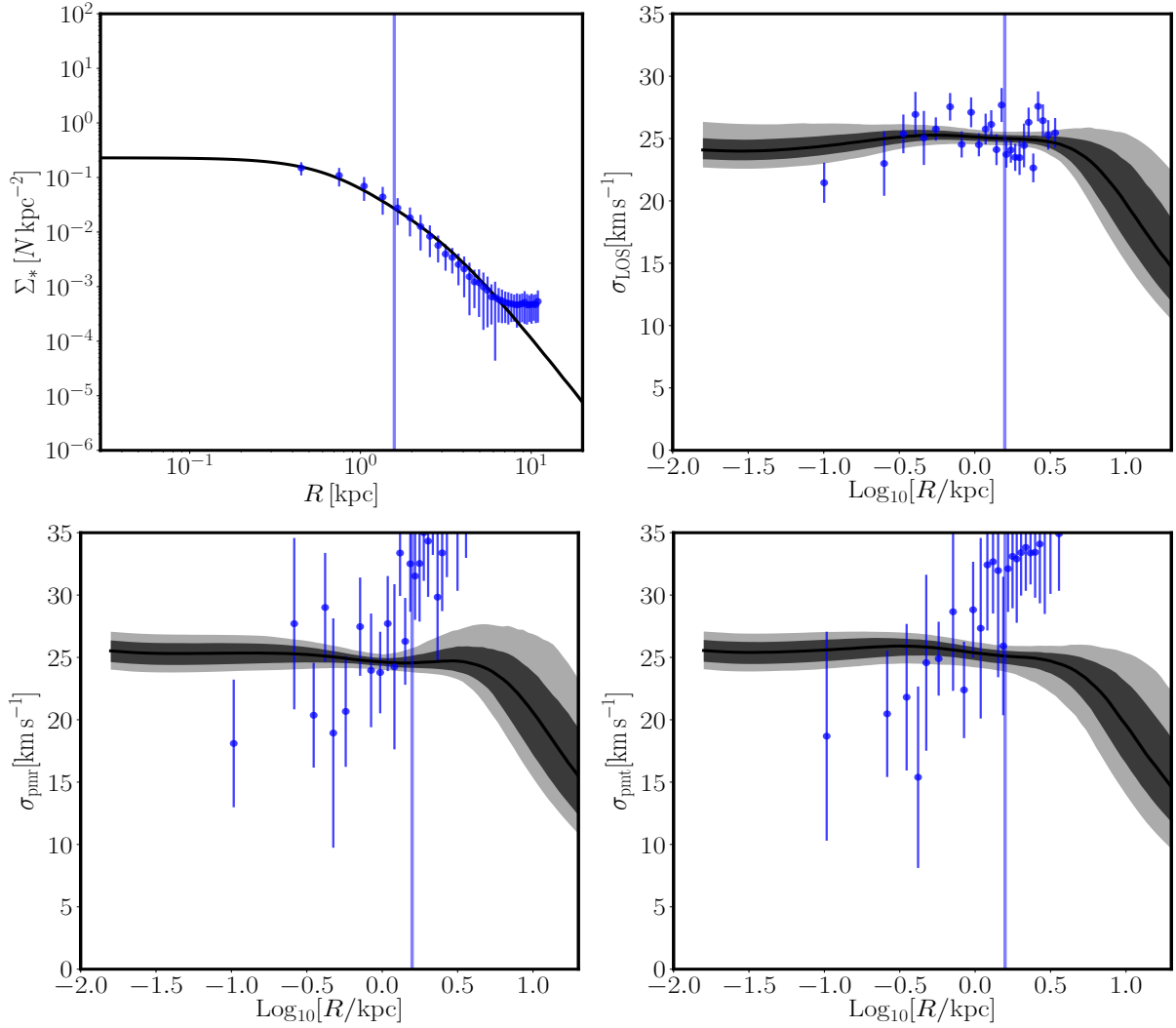


Figure A2. GRAVSPHERE recovered profiles for the real SMC. *Top left panel:* surface brightness $\Sigma_*(r)$. The black line is the GRAVSPHERE fit, the blue points with errorbars are the observed SMASH data and the faint blue line marks the half-light radius computed by GRAVSPHERE. *Top right panel:* velocity dispersion profile along the line of sight σ_{LOS} , the black line is GRAVSPHERE best fit solution, the dark and light grey contour are respectively the 68% and the 95% confidence intervals, the blue points with error bars are the binned data and the faint blue line marks the half-light radius computed by GRAVSPHERE. *Bottom left panel:* velocity dispersion profile along the radial direction σ_{rad} , lines and symbols are the same as for σ_{LOS} . *Bottom right panel:* velocity dispersion profile along the tangential direction σ_{tan} , lines and symbols are the same as for σ_{LOS} .

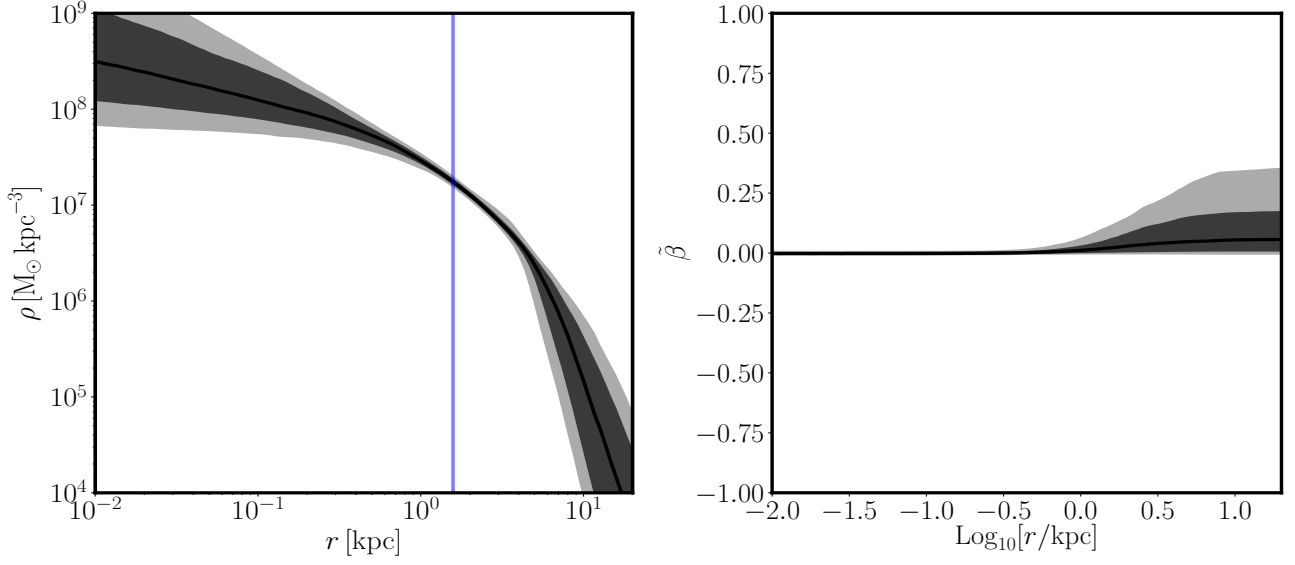


Figure B1. Same as Fig. 9: the mass density profile, $\rho(r)$, (left panel) and the symmetrised anisotropy profile, $\tilde{\beta}(r)$, (right panel) recovered by GRAVSPHERE for the SMC data but for a model with prior $-0.01 \leq \beta_0 \leq 0.01$.

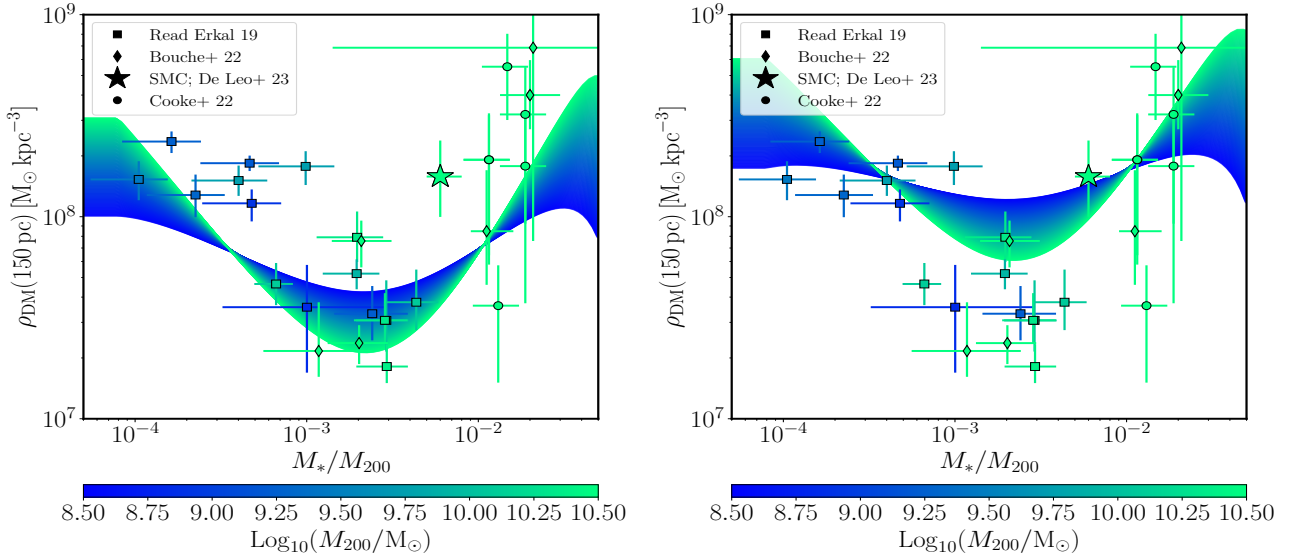


Figure C1. Side by side comparison of the base prediction of the Di Cintio et al. (2014b) model (left panel, same as the top right corner of Fig. 12) and the same model but factoring an hypothetical c_{200} bias. Notice how the bias in the estimation of the concentration parameter can reconcile the model with some of the highest density dwarfs (including the SMC)